Word Count: 11532; Revision 1

Mineral precipitation sequence from multi-stage fluids released by eclogite during high-pressure metamorphism

Ting-Nan Gong[1,2,3], Jin-Xue Du[1*], Li-Fei Zhang[2], Zhen-Yu Chen[4], Ze-Ming Zhang[1,5], Wei-(RZ) Wang[3], Yuan-Ru Qu[6]

[1]*School of Earth Sciences and Resources, China University of Geosciences, Beijing 100083, China*

[2]*MOE Key Laboratory of Orogenic Belts and Crustal Evolution, School of Earth and Space Sciences, Peking University, Beijing 100871, China*

[3]*Key Laboratory of Paleomagnetism and Tectonic Reconstruction of Ministry of Natural Resources, Institute of Geomechanics, Chinese Academy of Geological Sciences, Beijing 100081, China*

[4]*MNR Key Laboratory of Metallogeny and Mineral Assessment, Institute of Mineral Resources, Chinese Academy of Geological Sciences, Beijing 100037, China*

[5]*Institute of Geology, Chinese Academy of Geological Sciences, Beijing 100037, China*

[6]*State Key Laboratory of Geological Processes and Mineral Resources, China University of Geosciences, Beijing 100083, China*

*Corresponding author: Jin-Xue Du; E-mail address: jxdu@cugb.edu.cn

Abstract

Arc magmas above subduction zones hold abundant fluid-mobile elements attributed to fluids released from the dehydrating subducted oceanic crust. However, the quantity of trace elements in the fluids and their evolution with the metamorphic processes during subduction and exhumation are still unclear. The precipitation sequence of vein minerals preserves the nature of multi-stage high-pressure (HP) metamorphic fluids and the fingerprint of mass exchange in deep subduction zones. In this contribution, we conducted detailed petrological studies and phase equilibria modeling on a unique HP omphacite-rich vein and its host eclogite from the Chinese southwestern Tianshan. The host eclogite consists mainly of garnet, omphacite, epidote, glaucophane, phengite, quartz, and rutile. Garnet in the eclogite records prograde subduction and early exhumation characterized by decompression heating at P-T conditions of ~2.4–2.6 GPa and 460–540 °C. The embedded omphacite-rich vein has similar mineral assemblage to the host eclogite. Garnet grains in this vein are predominantly distributed along or intersect the vein wall, which record similar eclogite-facies metamorphic conditions to that of the host eclogite. Omphacite is dominant in the vein, while epidote and glaucophane occur interstitially. Phase equilibria modeling reveals a sequential growth of garnet-dominated, omphacite-dominated, and epidote-dominated assemblages from fluids originating from the breakdown of different hydrous minerals. These lines of evidence suggest that the formation of multi-stage HP fluids are a continuous long-term process with a spontaneously short-distance transport and sequential mineral precipitation. Calculated fluid compositions demonstrate that the fluids released by lawsonite breakdown during exhumation have great potential to modify the trace element systematics of arc magmas. Our findings reveal the nature and evolution of multi-stage HP metamorphic fluids from internal sources during subduction and exhumation of oceanic crust, providing valuable insights into the chemical compositions of arc magmas.

Keywords: metabasite; subduction zone; high-pressure fluid; arc magma; material cycle

Introduction

Subduction zones are the primary regions for mass and energy exchange between the Earth's interior and surface (e.g., Spandler and Pirard 2013; Zheng 2019; Ague et al. 2022; Li et al. 2022). High-pressure (HP) fluids released by dehydration of subducted slabs have been widely considered as a crucial medium for material cycling between the crust and the mantle at the convergent plate margins (e.g., Kessel et al. 2005; John et al. 2008; Li et al. 2020). Such material cycling mainly contributes to the infiltration of dehydrated fluids from subducting plates into the mantle wedge, inducing arc magmatism, and bring a portion of subducted crustal materials to the surface. Veins in HP and ultrahigh-pressure (UHP) metamorphic rocks are principal indicators of the past fluid flow and preserve natural information on the regime and composition of the fluid in subduction zones (e.g., Gao et al. 2007; Li et al. 2013, 2017a, 2021; Zhang et al. 2016; Cruz-Uribe et al. 2021). Zoned mineral textures and multi-facies mineral generations in complex metamorphic veins indicate the continuous and multi-step processes of mineral crystallization (e.g. Gao et al. 2007; Chen et al. 2012; Lü et al. 2012a; Angiboust et al. 2017). Clarifying the precipitation and crystallization order of various minerals within the vein space is conducive for understanding the evolution of metamorphic fluid and mass transfer from the subducting slab into the mantle wedge, e.g., the origin of fluid-mobile elements of arc magmas. However, mineral assemblages from different stages in HP veins have often been treated as a whole during petrological and geochemical studies to reflect the element migration at a specific metamorphic stage (e.g., Guo et al. 2012; Li et al. 2017a), and the detailed mineral-forming processes in the veins as well as the nature of related multi-stage fluids have received less attention.

The Chinese southwestern Tianshan (U)HP metamorphic belt is a typical cold oceanic subduction zone

(Zhang et al. 2008; Bayet et al. 2020). Numerous omphacite-dominated, garnet-dominated, epidote-dominated, rutile-dominated and quartz-dominated HP veins are observed on centimeter to meter scales within host metabasites (e.g., Gao et al. 2007; John et al. 2008, 2012; Beinlich et al. 2010; Lü et al. 2012a; Zhang et al. 2016), implying the flow of multi-stage fluids during HP-UHP metamorphism. Based on previous studies on the metamorphic evolution of metabasite-vein systems, aqueous fluids in subduction zones can be classified into prograde, peak-pressure, and retrograde fluids (e.g., Gao et al. 2007; van der Straaten et al. 2008). Previous studies proposed that the major pulses of prograde and peak-pressure fluid released by various hydrous minerals during the transformation from low-grade blueschist to dry eclogite, triggered partial melting of the overlying mantle wedge and mass transfer into arc magmas (Beinlich et al. 2010; John et al. 2012; Li et al. 2013). Similarly, retrograde fluids may facilitate rehydration of eclogite minerals back into blueschist assemblages (John et al. 2008; van der Straaten et al. 2008, 2012; Li et al. 2017a). However, the detailed formation stages of the dominant minerals in equilibrium in HP veins and the contribution of the related fluids to the composition of arc magmas remain poorly understood, and no systematic mineral precipitation sequences in the fluid pathway have been proposed.

To enhance further comprehension of the nature and evolution of metamorphic aqueous fluid, petrological study and phase equilibria modeling were conducted on a centimeter-scale omphacite-rich vein and the host glaucophane-epidote eclogite within the Chinese southwestern Tianshan (U)HP metamorphic belt. The results reflect the formation and evolution of internally-derived fluids and the multi-stage precipitation sequence of minerals in the fluid pathway. In conjunction with in-situ geochemical analyses, we attempt to unravel fluid composition of each stage and its possible geochemical contribution to arc magmas.

In this paper, the term glaucophane-epidote eclogite is used for such a low-temperature high-pressure metabasite (Tsujimori and Ernst 2014), although typical eclogite is restricted to a plagioclase-free rock with >75 vol.% of garnet + omphacite (Desmons and Smulikowski 2004). The mineral abbreviations are after Whitney and Evans (2010).

Geological Settings

The South Tianshan orogenic belt is located in Central Asia and extends over 2500 km from Uzbekistan, Tajikistan, Kyrgyzstan, and Kazakhstan to northwestern China along the southwestern margin of the Central Asian Orogenic Belt (Fig. 1; Tagiri et al. 1995; Gao et al. 1998, 1999; Volkova and Budanov 1999). The Chinese southwestern Tianshan (U)HP metamorphic belt is wedge-shaped with a maximum width of 30 km and is situated 200 km southwest of the South Central Tianshan Suture between the Central Yili Block and the Tarim Block (Fig. 1). This belt primarily consists of strongly schistose metasedimentary rocks, metabasites and marbles with minor ultramafic rocks (Gao et al. 1999; Zhang et al. 2002a, 2002b; Tan et al. 2017). Metabasites, including eclogites and blueschists, occur as enclosed lenses, massive or layered blocks of varying sizes within host metasedimentary rocks. Eclogites and blueschists are chemically characterized by normal mid-ocean ridge basalt (N-MORB), enriched mid-ocean ridge basalt (E-MORB), ocean island basalt (OIB), and arc basalt signatures (Zhang et al. 2001, 2007; Gao and Klemd 2003; Ai et al. 2006; John et al. 2008), representing relicts of the palaeo-Tianshan ocean (Klemd et al. 2015; Tan et al. 2019; Zhang et al. 2019).

Ubiquitous HP vein networks have been documented in metabasites from the Chinese southwestern Tianshan (U)HP metamorphic belt (e.g., Gao and Klemd 2001; Lü et al. 2012a; Zhu et al. 2020). These veins were formed by the dehydration of previous hydrous minerals and represented re-mineralization products from internally or externally derived HP-UHP fluids (Zack and John 2007; John et al. 2008). This is compatible with studies on primary fluid inclusions (e.g., Gao and Klemd 2001), which also displays direct evidence for large-scale fluid/rock interactions in this terrane.

Analytical Methods

Major element compositions of minerals were determined at the Ministry of Natural Resources, Key Laboratory of Metallogeny and Mineral Assessment, Institute of Mineral Resources, Chinese Academy of Geological Sciences, with a JEOL JXA-8230 Electron Probe Micro Analyzer (EPMA) equipped with four wavelength-dispersive spectrometers. The samples were firstly coated with a ca. 20 nm thin conductive carbon film prior to analysis. An accelerating voltage of 15 kV, a beam current of 20 nA, a peak-count time of 10 seconds and a 5 μm spot size (2 μm for some tiny inclusion minerals) were performed for analyzing. Natural minerals and synthetic oxides were used as standards. Data were corrected on-line using a modified ZAF (atomic number, absorption, fluorescence) correction procedure. Relative analytical uncertainties are <2% for major elements.

Trace element compositions of minerals were determined using Laser Ablation Inductively Coupled Plasma Mass Spectrometry (LA-ICP-MS) at the In-situ Mineral Geochemistry Lab, Ore deposit and Exploration Centre (ODEC), Hefei University of Technology, China. The analyses were carried out on an Agilent 7900 Quadrupole ICP-MS coupled to a Photon Machines Analyte HE 193-nm ArF Excimer Laser Ablation system equipped. Argon was used as the make-up gas and mixed with the carrier gas via a T-connector before entering the ICP. Each analysis was performed by a spot size diameter of 30 μm at 8 Hz with the energy of ~4 J/cm^2 for 40s after measuring the gas blank for 20s. Standard reference materials NIST610, NIST612, and BCR-2G were used as external standards to plot the calibrated curves, running after each 10–15 unknowns. The off-line data processing was performed using ICPMSDataCal (Liu et al. 2008). Relative analytical uncertainties of most major and trace elements are <5% and <10%, respectively.

An automated mineralogy approach has been adopted for phase/mineral and element distribution mapping obtained by a TESCAN Integrated Mineral Analyzer (TIMA) system at the Institute of Geology, Chinese

Academy of Geological Sciences, Beijing. The analyses were performed on the thin section with 25 kV accelerating voltage, 7.55nA beam current, 15 mm working distance, and 91.67 nm spot size.

Petrography

To explore the crystallization processes of vein minerals and geochemical characteristics of associated fluids, a typical eclogite-vein system (sample A300-12) was selected for detailed petrological studies (Figs. 2, 3).

Host eclogite

The host eclogite of sample A300-12 is a glaucophane-epidote eclogite and displays a massive structure and porphyroblastic texture (Fig. 2). This eclogite is mainly composed of garnet (15 vol.%), omphacite (23 vol.%), epidote (25 vol.%), glaucophane (22 vol.%), phengite (8 vol.%), quartz (4 vol.%) and rutile (3 vol.%), with accessory minerals including apatite, allanite, paragonite, and carbonates (most calcite and minor dolomite).

Garnet occurs as coarse-grained (1.0–1.5 mm in diameter) euhedral to subhedral porphyroblasts (Grt_E; Figs. 2b, c). It commonly develops an obvious core-rim texture (Fig. 2d). The core and mantle contain a large number of primary inclusions (isolated and no obvious cracks around) of aegirine–augite (Figs. 2f, g), rutile, quartz, and aggregates of box-shaped epidote + paragonite ± chlorite (possible lawsonite pseudomorphs (Evans 1990; Figs. 2g, 3c), whereas the rim contains a few inclusions such as omphacite, quartz and rutile (< 20 μm; Figs. 2e, f).

Two types of clinopyroxene are present in the eclogite: omphacite and aegirine-augite (Aeg-Aug). Detailed petrographic studies show that (1) the rounded and light Aeg-Aug inclusions in BSE images occur in the garnet core and mantle (Figs. 2f, g), (2) the dark omphacite inclusions are distributed as patchy sectors in the garnet rim (Omp_{EG}-r; Figs. 2e, f) and occasionally in epidote, and (3) the anhedral fine-grained matrix omphacite is zoned with grey cores (Omp_{EM}-c with a few Aeg-Aug) and dark rims (Omp_{EM}-r; Fig. 2f). The growth sequence of clinopyroxene was identified as: Aeg-Aug→ Omp_{EG}-r and Omp_{EM}-c → Omp_{EM}-r.

Glaucophane usually occurs in the matrix, and tiny glaucophane relics are occasionally enclosed within matrix omphacite. Phengite displays an irregular or corroded shape in the matrix or adjacent to the garnet rims (Figs. 2e, f).

Epidote displays as rod-like porphyroblasts (0.5–1.5 mm in length and 0.1–0.2 mm in width) and two textural generations (Figs. 2e, h), with the early generation (core) being slightly lighter in BSE images than the later (rim). It occasionally contains omphacite, quartz, and rutile inclusions (Fig. 2h) and locally enclose allanite relicts in the inner portions.

Paragonite intergrown with epidote is enclosed in garnet and occurs in the matrix (Figs. 2g, 3), probably representing the product of breakdown of lawsonite (e.g., Barnicoat and Fry 1986; Lü et al. 2009). Tiny rutile is distributed in the matrix or trapped by garnet, and the former generally has a retrograde rim of titanite (Fig. 2h).

Omphacite-rich vein

The omphacite-rich vein is made up of omphacite (80 vol.%), garnet (10 vol.%), epidote (3 vol.%), phengite (5 vol.%), quartz (2 vol.%), and minor mineral phases such as glaucophane, apatite, dolomite, and calcite. The contact wall between the vein and its host eclogite is well defined and no alteration selvages or transition zones were found (Figs. 2a, b).

A considerable amount of large idioblastic garnet porphyroblasts grew at the eclogite-vein wall both into the vein and the host eclogite ($Grt_{V\text{-}E}$; Figs. 2b, c, j), with a small amount independently in the vein channel

(Grt_V). Grt_V has a similar grain size, shape, and zoning profile to Grt_E. However, the feature of its inclusions is significantly different from that of Grt_E (Fig. 3): the core of Grt_V is usually inclusion-free, whereas abundant inclusions, such as omphacite, quartz, and epidote + paragonite exist in its mantle, and the quantity of these inclusions decreases towards the rim (Fig. 3a). Two sides of $Grt_{V\text{-}E}$ are characterized by Grt_E and Grt_V (Fig. 3), respectively. Omphacite occurs as the major phase of the vein, displaying widely irregular and zigzag textures (Fig. 2i). Vein omphacite in the matrix (Omp_{VM}) consistently exhibits a light core (Omp_{VM}-c; some are Aeg-Aug), overgrown by a dark rim (Omp_{VM}-r) in the BSE image (Fig. 2i). Similar to the host eclogite, aegirine-augite also exists as inclusions in the mantle of Grt_V (Fig. 2j). Phengite occurs as fine-grained aggregates in the vein. Epidote and glaucophane usually grow in the central section of the vein, and fill voids between omphacite crystals. Locally, omphacite and quartz inclusions are observed in apatite and epidote grains. Minor quartz is scattered in the vein. Rutile and titanite are not observed.

Mineral Chemistry

Representative major and trace element compositions of minerals are listed in Table S1 and S2 and shown in Figs. 4 and 5.

Garnet

For major elements, Grt_E and Grt_V display similar profiles (Figs. 4a, 5): from core to rim of both Grt_E and Grt_V, the Sps (spessartite) content bell-shaped decreases while the Prp (pyrope) content gradually increases, indicative of well-developed growth zoning (Spear 1995); the Alm (almandine) content subtly increases to the mantle and then sharply decreases to the rim, whereas the Grs (grossular) content remains almost constant except a subtle increase in the rim. Grt_E shows a wide compositional range with a Mg-poor and Mn-rich core of $Alm_{69.5\text{-}70.2}Grs_{18.9\text{-}20.0}Prp_{3.6\text{-}3.9}Sps_{6.6\text{-}8.0}$, a Fe-rich mantle of $Alm_{72.9\text{-}73.8}Grs_{19.3\text{-}20.7}Prp_{5.0\text{-}6.3}Sps_{1.1\text{-}1.2}$ and a Mgrich and Mn-poor rim of $Alm_{64.3\text{-}65.6}Grs_{21.1\text{-}23.5}Prp_{10.4\text{-}12.6}Sps_{<1}$ (Table S1 and Figs. 4a, 5g-i). Similarly, Grt_V exhibits a zoning with a core of $Alm_{69.2\text{-}70.7}Grs_{19.3\text{-}20.4}Prp_{3.6\text{-}4.8}Sps_{6.2\text{-}6.4}$, a mantle of $Alm_{71.1\text{-}72.9}Grs_{19.3\text{-}20.6}Prp_{5.8\text{-}9.5}Sps_{0.7\text{-}1.4}$ and a rim of $Alm_{64.2\text{-}64.8}Grs_{21.1\text{-}23.7}Prp_{11.1\text{-}12.5}Sps_{<1}$ (Table S1 and Figs. 4a, 5a-c). Even for $Grt_{V\text{-}E}$, the compositions on both sides of the garnet are similar (Fig. 5d-f).

In chondrite-normalized rare earth element (REE) diagrams (Fig. 6a-d), both Grt_E and Grt_V display LREE-depleted and HREE-enriched signatures. The cores have higher HREE and Y contents compared to the rims (e.g., 245 ppm Yb and 950 ppm Y vs. 4.1 ppm Yb and 63.7 ppm Y; Fig. 6a-d, Table S2). They contain high concentrations of transition metal elements of Sc (9.5–77.9 ppm), V (36.0–88.4 ppm), Co (21.3–69.8 ppm), and Zn (23.0–91.0 ppm). For Grt_V, both the large ion lithophile elements (LILEs) and the high field-strength elements (HFSEs) are of low amount, of which LILEs show a slight decrease from core to rim (e.g., 5.05 → 0.23 ppm for Rb) while HFSEs a slight increase (e.g., 0.27 → 1.43 ppm for Zr).

Clinopyroxene

According to the WEF (wollastonite + enstatite + ferrosilite) -Jd (jadeite) -Aeg (aegirine) diagram (Morimoto 1989; Fig. 4b), most clinopyroxenes in the host eclogite and the vein are omphacite, while some matrix clinopyroxene cores and clinopyroxene inclusions in garnet fall within the compositional range of aegirine-augite. Clinopyroxenes vary slightly in Na (most in the range of 0.50–0.64 p.f.u.) but widely in X_{Al} (=$Al/(Al+Fe^{3+})$; 0.27–0.96). The clinopyroxene inclusions within core/mantle of Grt_E and Grt_V share a similar low-Al and high-Fe^{3+} compositional range ($WEF_{30\text{-}51}Jd_{18\text{–}33}Aeg_{27\text{-}46}$), whereas, the clinopyroxene inclusions in the rims of Grt_E and Grt_V shows a high-Al and low-Fe^{3+} composition ($WEF_{38\text{-}50}Jd_{24\text{–}39}Aeg_{16\text{-}33}$; Fig. 4b; Table S1). Matrix clinopyroxene in the host eclogite shows a higher X_{Al} (0.46-0.96; $WEF_{37\text{-}53}Jd_{23\text{–}49}Aeg_{2\text{-}29}$) than that in the vein (0.35-0.82; $WEF_{30\text{-}48}Jd_{22\text{–}47}Aeg_{9\text{-}46}$), and both exhibit an obvious increase of X_{Al} from core to rim

(Fig. 4b).

Omphacite in the eclogite and the vein display similar concentrations of Li (22–57 ppm), Sc (17–101 ppm), Co (24–44 ppm), Zn (117–174 ppm), Ga (15–29 ppm), and Sr (13–30 ppm), whereas, Omp_{EM} (the omphacite in eclogite matrix) shows higher Cr (182–193 ppm) and V (341–357 ppm) than Omp_{VM} (8–96 ppm for Cr and 211–318 ppm for V; Table S2).

Glaucophane

According to Leake et al. (1997), all analyzed amphiboles are classified as glaucophane with Na_A = 0–0.04 p.f.u., Al^{IV} < 0.1 p.f.u. and Al^{VI} = 1.6–1.8 p.f.u.. Glaucophane in the host eclogite has higher Na_B (1.85–1.92 p.f.u.) than that in the omphacite-rich vein (Na_B=1.67–1.80 p.f.u.; Fig. 4c; Table S1), while both glaucophanes display a slight decrease of $Mg/(Mg+Fe^{2+})$ from core (0.63–0.70) to rim (0.59–0.63; Fig. 4c).

For trace elements, glaucophanes in both the host eclogite and the vein have high concentrations of transition metal elements (i.e., V: 124–318 ppm, Co: 84–146 ppm, Ni: 249–691 ppm, and Zn: 291–494 ppm; Table S2) and low Li (19–39 ppm), Sc (2–22 ppm) and Ga (9–15 ppm) contents. Compared with the eclogite glaucophane, the vein glaucophane generally has lower Cr content (30–41 ppm vs. 105–189 ppm).

Epidote and allanite

Epidote porphyroblasts of both the host eclogite and the vein generally develop a compositional zoning (Fig. 4d). The rims have higher X_{Fe} ($X_{Fe}=Fe^{3+}/(Fe^{3+}+Al)$) values (0.24–0.28) than the cores (0.17–0.19). Epidote inclusions in garnet show a wider X_{Fe} (0.16–0.31). Most epidote grains have relatively high Sr (2134–2231 ppm), Y (44–53 ppm), V (424–493 ppm), Ga (63–67 ppm), and LREE (27–93 ppm for La) concentrations (Table S2; Fig. 7a). In the chondrite-normalized REE patterns (Fig. 6e), epidote shows an LREE-rich pattern, in which vein epidote has a significant positive Eu anomaly.

Allanite occurs as only the core of epidote porphyroblasts in the host eclogite, with small grain sizes and less measurable data. Analyzed allanite grains have the highest Sr (up to 9680 ppm), Pb (up to 164 ppm), Th (up to 439 ppm), U (up to 76 ppm), and LREE (up to 4097 ppm for La) contents among all minerals from the eclogite and the vein in this study, and also has relatively higher concentrations of Sc, V, Cr, Zn, Ga and Ge with minor Co, Ni, Cu and Zr (Table S2; Fig. 7a). Likewise, the REE pattern of allanite displays strong enrichment in LREE with respect to HREE (Fig. 6e).

White mica

Phengite in the eclogite and the HP vein has variable but high Si contents of 3.4–3.7 p.f.u., with an average Si value ($Si_{average}$) of 3.505 p.f.u., and high Ba (2195–2778 ppm), Rb (243–278 ppm), and Cs (5.8–6.6 ppm) contents (Tables S1, S2). It contains considerable amounts of Li (4–14 ppm), V (125–279 ppm), Co (21–36 ppm), Ni (73–152 ppm), Zn (92–145 ppm), and Ga (29–58 ppm). The Cr content of phengite in the host eclogite (142–250 ppm) is significantly higher than that in the vein (11–86 ppm). Paragonite is close to the ideal composition of the pure end-member $Na\{Al_2[AlSi_3O_{10}](OH)_2\}$.

Apatite

Apatite in the eclogite and the HP vein has a high F content (2.2–2.8 wt.%) and a low Cl content (<0.1 wt.%; Table S1). Apatite in the vein typically contains considerable amounts of Sr (2419–3602 ppm), variable Y (159 → 11 ppm from core to rim), and REEs (23.8 → 0.7 ppm from core to rim for La; Table S2; Figs. 6f, 7b). Its REE patterns show enrichment in LREE-MREE, especially MREE (Fig. 6f).

Titanite and rutile

Titanite has a uniform composition of SiO_2 (30–32 wt.%), TiO_2 (32–35 wt.%), CaO (26–28 wt.%), Al_2O_3 (1–2 wt.%), FeO (<2.0 wt.%), and F (0.3–0.4 wt.%).

Rutile from the eclogite has a formula close to the ideal one of TiO_2, with minor Fe_2O_3 (0.3–0.7 wt%), and contains V of 612–977 ppm, Cr of 262–291 ppm, Zr of 24–91 ppm, Nb of 1308–1620 ppm, Ta of 71–155 ppm and Hf of 0.5–1.0 ppm. The Nb/Ta ratio is ~10-18.

Phase Equilibria Modeling and P-T Conditions

To constrain the P-T conditions of the eclogite-vein system and characterize the breakdown of hydrous minerals, phase equilibria modeling is developed on the host eclogite. The phase equilibria was modeled using the Domino/Theriak software (de Capitani and Petrakakis 2010) together with the internally consistent thermodynamic dataset ds55 (Holland and Powell 1998) in the system of MnNCKFMASHOTi (MnO-Na_2O-CaO-K_2O-FeO-MgO-Al_2O_3-SiO_2-H_2O-O-TiO_2). P_2O_5 and CO_2 were ignored, since they are mainly stored in accessory apatite and calcite, respectively, and also the fluid in cold subduction zones is known to have low CO_2 content (Molina and Poli 2000; Tian and Wei 2014). H_2O was put in excess due to the widespread occurrence of hydrous minerals such as epidote, glaucophane, paragonite, and phengite. Activity-composition relationships used in the modeling are as follows: chlorite, epidote, and talc (Holland et al. 1998); garnet and biotite (White et al. 2005); clinopyroxene (Green et al. 2007); amphibole (Diener et al. 2007); paragonite and phengite (Coggon and Holland 2002); feldspar (Holland and Powell 2003; Baldwin et al. 2005). Quartz, coesite, lawsonite, rutile, titanite, and aqueous fluid (H_2O) are treated as pure end-members.

The P-T pseudosection for the eclogite was calculated using the effective bulk-rock composition (Si:46.32, Ti:2.82, Al:17.96, Fe:10.52, Mn:0.11, Mg:5.68, Ca:9.99, Na:5.98, K:0.61, O:156.24 and excess H_2O; mol.%) estimated from percentage content (constrained by TIMA) and EPMA data of each mineral, with a P-T range of 400–600 °C and 10–30 kbar (Fig. 8). The assemblage of garnet + clinopyroxene is stable over most of the P-T range except at a few areas below 15 kbar (Fig. 8a). The observed matrix mineral assemblage of garnet

+ omphacite + glaucophane + epidote + phengite + quartz + rutile corresponds to a wide field of 13–21 kbar and 500–590 °C. Compositional isopleths have been calculated for Si in phengite (3.2–3.8 p.f.u.), Grs (20–40 mol.%), and Prp (3–18 mol.%) in garnet (Fig. 8b). The measured core-rim profile of Grt_E (yellow to red points in Fig. 8a) reflects a clockwise P-T vector from ~25 kbar at 460 °C, through ~26 kbar at 480 °C (the peak pressure conditions (P_{peak})) to ~24 kbar at 540 °C (the peak temperature conditions (T_{peak})) in the field of garnet + clinopyroxene + glaucophane + lawsonite + phengite + quartz + rutile, in agreement with lawsonite pseudomorph observed in garnet (Figs. 2g, 3c). The average Si value of phengite in the matrix (3.505 p.f.u.) is consistent with the pressure (24 kbar) calculated by garnet rim compositions, indicating a thermal relaxation process after the P_{peak} stage. The euhedral texture and the absence of obvious retrograde overprinting of garnet (Figs. 2, 3, 5) may reflect an exhumation path with constant garnet modal content. Combining the matrix mineral assemblage (Fig. 8a) and the evolution of garnet modal content (Fig. S1a), isothermal decompression after T_{peak} stage is inferred for exhumation of the eclogite (Fig. 8a). As a summary, a clockwise P-T path from A to D (the dotted gray line with arrows in Fig. 8a) is predicted for the host eclogite.

For the stability of clinopyroxene, aegirine-augite (X_{Al}<0.5) exists at the stability fields of lawsonite less than ~540 °C, whereas omphacite (X_{Al}>0.5) is stable at higher temperatures (Fig. 8a). Such high critical temperature of phase transition is inconsistent with petrographic observations of aegirine-augite inclusions in garnet cores and omphacite inclusions in garnet mantles and rims (Figs. 2e, f). This may be caused by element fractionation during clinopyroxene growth. Taking into account such fractionation (formed clinopyroxene no longer participates in subsequent metamorphic reactions), aegirine-augite will transform into omphacite at lower temperatures (~520 °C; Fig. S1b).

The modal contents of water and major hydrous minerals are presented in Fig. 8c-f. They show that the modal content of water is highly controlled by lawsonite at low-temperature and high-pressure conditions, and glaucophane/chlorite at other conditions. To better constrain the variation in mineral modes and water content, we plotted the computed modal variations of major minerals and water content in solid phases along the inferred P-T path (Fig. 9). According to this model, during the prograde metamorphic stage from A to B, the total amount of H_2O in solid phases drops sharply from 18.2 to 13.8 mol.% (Figs. 8c, 9). All chlorite (0.4 mol.%) and a small amount of glaucophane (0.5 mol.%) and lawsonite (1.0 mol.%) broke down and released 1.8, 0.5, and 2.1 mol.% H_2O, respectively (Figs. 8c-f, 9). The initial growth of garnet (the dotted line in Fig. 9) was accompanied by consume of chlorite and lawsonite, whereas clinopyroxene grew by breakdown of lawsonite and glaucophane. During the thermal relaxation stage from B to C, the total amount of H_2O in solid phases continued to drop from 13.8 to 8.9 mol.% (Figs. 8c, 9) due to the breakdown of lawsonite (1.9 mol.% and released 3.6 mol.% H_2O) and glaucophane (1.3 mol.% and released 1.3 mol.% H_2O). Garnet, omphacite, and quartz continued to grow at this stage. During the isothermal decompression stage from C to D, lawsonite rapidly decomposed at ~19 kbar and was completely transformed into epidote (Figs. 8e, 9). The water content of the whole rock decreased rapidly from 8.9 to 4.1 mol.% with the decomposition of lawsonite (Figs. 8c, 9). After then, the modal content of glaucophane began to increase and that of omphacite started to decrease.

Discussion

Metamorphic evolution of the host eclogite

Based on the petrographic observations, mineral geochemical data, and phase equilibria modeling results described above, a clockwise P-T path along a low geothermal gradient (5-6°C/km) is identified for the host eclogite (Fig. 8a), which is comparable with that of eclogites coexisting with garnet blueschists from the central section of Atantayi valley (480-560°C and 22-27.5 kbar; Tian and Wei, 2014) and the lawsonite-bearing eclogite in the Habutengsu valley (490-570 °C and 20-26 kbar; Du et al. 2014a). Here we propose a three-stage metamorphic evolution of the host eclogite: (a) the prograde lawsonite blueschist-facies (Lws-BS facies) stage with compression heating, (b) the glaucophane lawsonite eclogite-facies (Gln-Lws-EC facies) stage with decompression heating, and (c) the glaucophane epidote eclogite-facies (Gln-Ep-EC facies) stage with isothermal decompression.

The prograde Lws-BS stage is characterized by Mg-poor garnet cores and their inclusions, e.g., rutile and aegirine-augite (Figs. 2, 3). Although lawsonite is not observed, box-shaped epidote + paragonite ± chlorite inclusions in garnet (Figs. 2g, 3c) infers the former presence of lawsonite (Evans 1990), in agreement with previous reports of lawsonite in eclogites from southwestern Tianshan (Li et al. 2013; Du et al. 2014a). The compositional isopleths of garnet cores point to ~460 °C and 25 kbar for this stage (Fig. 8a). The initial growth of garnet is directly driven by the decomposition of lawsonite and chlorite (Figs. 8, 9) via the following overall reaction (based on the change in the calculated mineral modal abundances, the same below; Fig. 9): Chl + Lws + Aeg-Aug + Qz = Grt + Gln + H_2O (1).

The metamorphic conditions of P_{peak} (~480 °C and ~26 kbar) are estimated by the mineral assemblage of garnet + clinopyroxene + glaucophane + lawsonite + phengite + quartz + rutile as well as the compositions of garnet cores and mantles (Fig. 8a). This condition corresponds to a geothermal gradient of 5–6 °C/km, which, again, confirms the cold oceanic subduction origin of the Chinese southwestern Tianshan (U)HP metamorphic belt (Lü et al. 2012b; Du et al. 2014a; Tan et al. 2019).

The early exhumation stage within the Gln-Lws-EC facies after P_{peak} is evidenced by the increase of Prp and Grs contents from the mantle to rim of garnet, omphacite inclusions (with Jd content < 50 mol.%) from garnet mantle and rim, and Si contents of phengite ($Si_{average}$ = 3.505 p.f.u.). Post-peak heating decompression (so-called thermal relaxation) is predicted by garnet compositions (Fig. 8a, b). Such heating process has also been widely observed in western Dabie (Xia et al. 2023), southwestern Tianshan (Zhang et al. 2019), South

DOI: https://doi.org/10.2138/am-2023-9218. http://www.minsocam.org/

Altyn (Dong and Wei 2021), and southern California (Dong et al. 2022), which may represent the slow exhumation of metabasite by their own buoyancy after subducting to ultimate self-exhumation depth (Yang et al. 2013; Du et al. 2014b; Wang et al. 2019; Zhang and Wang 2020), or reflect the upward mélange channel heating during trench retreat and slab steepening (Dong and Wei 2021; Dong et al. 2022). Further eclogitization is enhanced by continuing decomposition of lawsonite and glaucophane (Fig. 9) and the transition of aegirine-augite to omphacite (Figs. 8a, S1b), via the following overall reaction (Fig. 9): Gln + Lws = Aeg-Aug/Omp + Grt + Qz + H_2O (2).

The conditions of T_{peak} (~540 °C and ~24 kbar) are reflected by the garnet rim and phengite (Fig. 8a). The eclogite experienced subsequent isothermal decompression to ~13–20 kbar, characterized by the matrix mineral assemblage of garnet + omphacite + glaucophane + epidote + phengite + quartz + rutile. During this decompression process, indicated by our modeling results and numerous experimental and natural sample studies, a large amount of fluid was released during the transition from lawsonite to epidote (Figs. 2g, 8, 9; Clarke et al. 2006; Orozbaev et al. 2015), via the following reaction (Fig. 9): Omp + Lws + Grt = Ep + Gln + Qz + H_2O (3).

Mineral precipitation sequence in the fluid pathway

The formation and evolution of HP veins are dominantly controlled by internal properties (fluid composition, fluid flux, mineral solubility, etc.) and significantly affected by external factors (P-T conditions, stress, subduction rate, etc.). In general, the formation of HP vein networks resulting from prograde dehydration processes often begins with dehydration veins (Gao and Klemd 2001) and progresses to transport veins (Castelli et al. 1998; John et al. 2008). The transport veins are produced with the long-distance migration and infiltration of external fluids (John et al. 2008). The small-scale (centimeter to millimeter in width; Fig. 2), similar mineral assemblage and mineral chemistry to the host eclogite (Fig. 4, Table S2), and no reaction selvage of the omphacite-rich vein studied here suggest that the fluid represented by sample A300-12 stemmed from an internal source transported only for short-distance (dehydration vein; e.g., Spandler et al. 2011; Zhang et al. 2016).

The minerals precipitated in HP veins are a function of their solubilities in metamorphic fluids and their Gibbs Free Energy differences from those in the host eclogites. Actually, any mineral available in the host eclogites may be present in the internally-derived veins (e.g. Li et al. 2021). The mineral species of the studied omphacite-rich vein is a subset of the host eclogite (Fig. 2). Furthermore, textural relationship indicates a rough and apparent sequence for precipitation of vein minerals (Figs, 2, 3, 5), namely, garnet core (denoted as garnet-dominated assemblage), garnet mantle/rim + aegirine-augite/omphacite (omphacite-dominated assemblage) to epidote + glaucophane (epidote-dominated assemblage), which probably corresponds to the three metamorphic stages of the host eclogite and represents products of Reactions 1, 2 and 3, respectively. Migration and precipitation of phengite, apatite, calcite and dolomite, which are proposed to have not been involved in any reaction (Fig. 9), may be attributed to high solubilities of themselves (e.g., calcite/aragonite; Lan et al. 2023) or relevant elements (e.g., K and P; Sokol et al. 2023) in fluids. The precipitation sequence of vein minerals, combined with the metamorphic history of the host eclogite, is illustrated in Fig. 10 to demonstrate the genesis of the rock-vein system. During prograde metamorphism, high pore-fluid pressure and dehydration embrittlement of the rock formed on account of the release of the ongoing fluid (S1 and S2 in Fig. 10; Hacker et al. 2003; Jung et al. 2004). Further increase of fluid flux led to enhanced microfractures and channelized the fluid flow within the dehydration domain (Philippot and Selverstone 1991; Davies 1999; John et al. 2008), which is supported by the sharp contact between the vein and the host eclogite (Figs. 2a, b) and HP breccias in this belt (Wu and Xiao 2023). Garnet nucleated simultaneously in the eclogite and on the wall of fluid pathway when the P-T conditions reached its stable field (Fig. 8; S3 in Fig. 10). The inclusion-free core of vein garnet and the aegirine-augite-rich core of eclogite garnet serve as proof of this stage (Figs. 2, 3, 5). At the P_{peak} stage (S4 in Fig. 10), omphacite began to grow in the host eclogite and the vein, and eventually occupied the vein entirely. Garnet continued precipitating and omphacite evolved from aegirine-augite-rich composition to jadeite-rich one until the T_{peak} stage (S5 in Fig. 10, Fig. 4b). During the subsequent decompression process (S6 and S7 in Fig. 10), epidote (as well as glaucophane in the vein) successively filled the remaining spaces in the eclogite and the vein (Figs. 2b, 8a, 9).

Similarly, based on field and petrographic characteristics, possible precipitation sequences of vein minerals can also be predicted for previously reported dehydration HP veins from Chinese southwestern Tianshan, such as omphacite (→epidote) → quartz → rutile (Gao et al. 2007), and omphacite → epidote (Lü et al. 2012b; Li et al. 2013). Although such sequences may be somewhat inaccurate and require further research, they witness a continuous and multi-stage rather than a single-stage fluid evolution during the subduction-exhumation process of oceanic crust. Besides, cross-cutting relationship between veins can also be an effective way to clarify the fluid evolution. For instance, abundant monomineralic veins in the Mt. Emilius klippe (western Alps), developed during prograde to peak lawsonite eclogite facies, show that a garnet-dominated domain was first cut by a clinopyroxene-dominated vein, and both were cut by a clinozoisite vein (Angiboust et al. 2017). Such observations indicate a similar manner of fluid evolution and vein development (garnet → clinopyroxene → epidote) to our studies, showing the close correlation between mineral assemblages of veins and metamorphic processes of the host rock.

Nature of multi-stage fluids

Fluid composition is constantly changing during metamorphic evolution as a result of dissolution and crystallization of different minerals (Figs. 8, 9, 10). To explore nature of multi-stage HP fluids, the partition coefficients of trace elements for garnet, clinopyroxene, and epidote in aqueous fluids were adopted (Green and Adam 2003; Martin et al. 2011; Feineman et al. 2007; Rustioni et al. 2021), assuming chemical equilibrium between fluid and vein minerals at each stage. The three main stages during vein mineral precipitating are denoted as stages 1-3 (Figs. 11, S2). For stage 2, fluid composition was estimated by both aegirine-augite/omphacite and mantle/rim of garnet in the vein. Although a few elements (such as V and Ga; Fig. S2) show a slight inconsistence, most elements display comparable concentrations constrained by mantle/rim of garnet and clinopyroxene (Figs. 11, S2). For stages 1 and 3, fluid compositions were estimated by core of garnet and epidote respectively. Glaucophane, however, was not considered as relevant partition coefficients between it and fluid are not available.

Fluids at stage 1 and stage 2, from which core of garnet and aegirine-augite/omphacite + mantle/rim of garnet in the vein were precipitated, show similar trace element compositions (Figs. 11, S2). They are both characterized by the enrichment of LILEs (e.g., Rb), Y, Pb and transition metal element V and Ga (most above 1 ppm), and the depletion of most other elements (most below 0.1 ppm). However, most elements show a decrease of concentrations from stage 1 to stage 2. According to Reactions 1 and 2, fluids at these two stages are mainly released by dehydration of chlorite and glaucophane, respectively, as well as lawsonite (Figs. 8, 9). Chlorite and glaucophane are proposed to contain low concentrations of most trace elements (Spandler et al. 2003) while lawsonite is the main host mineral of LILEs, REEs and Pb in eclogites (Green and Adam 2003; Martin et al. 2011, 2014; Zheng et al. 2016). As a result, the enrichment of LILEs, Y, and Pb could be attributed to the breakdown of lawsonite. The depletion of other elements, on the other hand, may result from the crystallization of garnet and allanite which prefer to HREEs and LREEs (Fig. 6) respectively (Green and Adam 2003; Spandler et al. 2003).

In equilibrium with epidote and glaucophane, fluid at stage 3 displays a significant enrichment of the majority of trace elements (e.g., LILEs and REEs; Figs. 11, S2). It shows much higher concentrations of most elements, some of which may be 3-4 order of magnitudes higher, than the former two stages (e.g. La and Sm; Figs. 11, S2). According to Reaction 3, fluid at this stage is mainly released by breakdown of lawsonite, and a large amount of solutes have been liberated during early exhumation (Figs. 9, 12), in accordance with the results of mass balance calculation for a retrograde albite–calcite vein from Chinese southwestern Tianshan (Li et al. 2017a). HP-UHP fluids enriched in large ion lithophile elements (e.g., Cs, Rb, Ba, and Sr), U, Th, and REE were also reported in the Makbal UHP Complex, the UHP Dabie terrane and the Sulu terrane, which is interpreted as breakdown or dissolution of lawsonite, phengite, carbonate and allanite/monazite during subduction and exhumation (Orozbaev et al. 2015; Ferrando et al. 2019; Tang et al. 2021). Our results indicate that the properties of metamorphic fluids during subduction and exhumation depend on the on-going decomposing minerals and the mineral assemblage in equilibrium with fluid at that time.

Implications

The infiltration of fluids released by subducted oceanic crust into the mantle wedge may potentially modify the chemical compositions of the hybridized mantle (Kessel et al. 2005; Spandler et al. 2007; Spandler and Pirard 2013; Ague et al. 2022). It is generally accepted that arc magmas have higher concentrations of LILEs and LREEs than mid-ocean ridge basalts (MORB), partially resulting from the involvement of slab-derived fluids (Tsay et al. 2014, 2017; Ferrando et al. 2019; Hernández-Uribe et al. 2020; Tang et al. 2021). Subduction-zone fluid could be transported to the source region of arc magma through disequilibrium and focused flow (Ikemoto and Iwamori 2014; Pirard and Hermann 2015). In order to evaluate the possible influence of the fluids on arc magmas, we compared the calculated fluid composition at each stage with average N-MORB and global continental and island arc basalts (Fig. 12). Despite that of LILEs (e.g., Ba), the concentrations of most trace elements in the first two stages are distinctly lower than or similar to those of N-MORB, suggesting inappreciable influence of fluids formed by dehydration of chlorite and glaucophane at previous stages on arc systems. On the contrary, the concentrations of Ba, U, Sr, and LREEs in fluid of stage 3 (in equilibrium with epidote) are notably higher than those of N-MORB. Previous studies predicted that the hard-to-observed lawsonite holds large amounts of fluid-mobile elements and water in the rocks from cold subduction zones (Spandler et al. 2003; Clarke et al. 2006). Our modeling results also show that lawsonite released a large fluid flux (74% of the total water in the system; Fig. 9) and completely decomposed during the subduction-exhumation processes (i.e., 52% of lawsonite breakdown at the epidote stable field during exhumation). This indicates that fluids released during exhumation are enriched in fluid-mobile elements with respect to those of subduction (Figs. 12, 13). Such exhumation-derived fluids may account for the paired seismic and electrical conductivity anomalies, as well as the formation of some ore deposits (Vry et al. 2010; White et al. 2015). It also could explain the decoupling of fluid release and trace element release (Spandler et al. 2003). Thus, we confirm that the infiltration of fluid released during the breakdown of lawsonite in metabasites into the arc mantle has great potential to modify the chemical compositions of arc magmas (Fig. 13).

HP fluids may escape the subduction system not only into the mantle wedge but also along the subduction interface (Fig. 13). In the latter case, infiltration of HP fluids will result in strong fluid-rock interaction processes. The escape of fluid would lead to a significant density increment and an accompanying volume reduction. For instance, the density of the studied eclogite is 3.26 g·cm^{-3} at 400 °C and 21 kbar and 3.43 g·cm^{-3} at 540 °C and 19 kbar (calculated using Domino/Theriak), corresponding to a ~5 % volume reduction. This volume reduction may be up to ~15 % for some mafic protoliths (Angiboust et al. 2017), and therefore, could contribute to formation of HP breccias in this belt (Wu and Xiao 2023). Meanwhile, fluid released during subduction and exhumation could continuously weaken the subduction plate, enhance creep rates and generate rheological instabilities, and potentially serve as a principal cause of intermediate-depth seismicity (Etheridge et al. 1984; Davies 1999; Hacker et al. 2003). Furthermore, infiltration and metasomatism of HP fluids in subduction channel can also trigger prograde eclogitization (e.g. Beinlich et al. 2010), retrograde alteration (e.g. Li et al. 2017a) or deviation of bulk-rock Sr isotopic compositions (e.g. Wang et al. 2017; Wu and Xiao 2023) of some rocks. For instance, Beinlich et al. (2010) reported an example of Ca-metasomatism-induced eclogitization of a Ca-poor blueschist, the prerequisite for which is the infiltration of a Ca-rich fluid. Such HP fluid released by lawsonite breakdown (e.g. fluid at stage 3 in this study) may be responsible for this process.

In conclusion, detailed petrological studies and phase equilibria modeling reveal a clockwise P-T path with decompression heating for the host eclogite. Along with this P-T path, we constructed a three-stage precipitation model to illustrate the formation of the embedded omphacite-rich vein and the nature of multi-stage fluids accompanied. Associated with calculated trace element compositions of fluids, our findings provide a new perspective for the contribution of exhumation fluids to arc magmas.

Acknowledgments

The authors would like to thank two anonymous reviewers for their insightful and constructive comments that greatly improved the manuscript, and editor Thomas Mueller for his efficient handling. This work was financially supported by the NSFC Original Exploratory Program (42150104). Sincerely acknowledge are given to Cheng-Yang Sun (China University of Geosciences, Beijing), Yi Cao (China University of Geosciences, Wuhan), Tian-Rui Wang (Chengdu University of Technology), Yang Li (Peking University), Jun-Qi Liang (China University of Geosciences, Beijing), and Hong Bao (China University of Geosciences, Beijing) for their assistance with revising and Ming-Ming Guo (China University of Geosciences, Beijing) for his help with TESCAN Integrated Mineral Analyzer (TIMA) analysis.

References

Ague, J.J., Tassara, S., Holycross, M.E., Li, J.-L., Cottrell, E., Schwarzenbach, E.M., Fassoulas, C., and John, T. (2022) Slab-derived devolatilization fluids oxidized by subducted metasedimentary rocks. Nature Geoscience, 15, 320–326.

Ai, Y., Zhang, L., Li, X., and Qu, J. (2006) Geochemical characteristics and tectonic implications of HP-UHP eclogites and blueschists in southwestern Tianshan, China. Progress in Natural Science, 16, 624–631.

Angiboust, S., Yamato, P., Hertgen, S., Hyppolito, T., Bebout, G.E., and Morales, L. (2017) Fluid pathways and high- *P* metasomatism in a subducted continental slice (Mt. Emilius klippe, W. Alps). Journal of Metamorphic Geology, 35, 471–492.

Baldwin, J.A., Powell, R., Brown, M., Moraes, R., and Fuck, R.A. (2005) Modelling of mineral equilibria in ultrahigh-temperature metamorphic rocks from the Anápolis-Itauçu Complex, central Brazil. Journal of Metamorphic Geology, 23, 511–531.

Barnicoat, A.C., and Fry, N. (1986) High-pressure metamorphism of the Zermatt-Saas ophiolite zone, Switzerland. Journal of the Geological Society, 143, 607–618.

Bayet, L., Agard, P., John, T., Menneken, M., Tan, Z., and Gao, J. (2020) Tectonic evolution of the Tianshan Akeyazi metamorphic complex (NW China). Lithos, 354–355, 105273.

Beinlich, A., Klemd, R., John, T., and Gao, J. (2010) Trace-element mobilization during Ca-metasomatism along a major fluid conduit: Eclogitization of blueschist as a consequence of fluid–rock interaction. Geochimica et Cosmochimica Acta, 74, 1892–1922.

Borg, L.E., Brandon, A.D., Clynne, M.A., and Walker, R.J. (2000) Re–Os isotopic systematics of primitive lavas from the Lassen region of the Cascade arc, California. Earth and Planetary Science Letters, 177, 301–317.

Castelli, D., Rolfo, F., Compagnoni, R., and Xu, S. (1998) Metamorphic veins with kyanite, zoisite and quartz in the Zhu-Jia-Chong eclogite, Dabie Shan, China. Island Arc, 7, 159–173.

Chen, R.-X., Zheng, Y.-F., and Hu, Z. (2012) Episodic fluid action during exhumation of deeply subducted continental crust: Geochemical constraints from zoisite–quartz vein and host metabasite in the Dabie orogen. Lithos, 155, 146–166.

Clarke, G.L., Powell, R., and Fitzherbert, J.A. (2006) The lawsonite paradox: a comparison of field evidence and mineral equilibria modelling. Journal of Metamorphic Geology, 24, 715–725.

Coggon, R., and Holland, T.J.B. (2002) Mixing properties of phengitic micas and revised garnet-phengite thermobarometers. Journal of Metamorphic Geology, 20, 683–696.

Cruz-Uribe, A.M., Page, F.Z., Lozier, E., Feineman, M.D., Zack, T., Mertz-Kraus, R., Jacob, D.E., and Kitajima, K. (2021) Trace element and isotopic zoning of garnetite veins in amphibolitized eclogite, Franciscan Complex, California, USA. Contributions to Mineralogy and Petrology, 176, 41.

Davies, J.H. (1999) The role of hydraulic fractures and intermediate-depth earthquakes in generating subduction-zone magmatism. Nature, 398, 142–145.

de Capitani, C., and Petrakakis, K. (2010) The computation of equilibrium assemblage diagrams with Theriak/Domino software. American Mineralogist, 95, 1006–1016.

Desmons, J., and Smulikowski, W. (2004) High P/T metamorphic rocks. In A systematic nomenclature for metamorphic rocks. Cambridge University Press, New York.

Diener, J.F.A., Powell, R., White, R.W., and Holland, T.J.B. (2007) A new thermodynamic model for clino- and orthoamphiboles in the system Na_2O-CaO-FeO-MgO-Al_2O_3-SiO_2-H_2O-O. Journal of Metamorphic Geology, 25, 631–656.

Dong, J., and Wei, C. (2021) Multi-Stage Metamorphism of the South Altyn Ultrahigh-Pressure Metamorphic Belt, West China: Insights into Tectonic Evolution from Continental Subduction to Arc–Backarc Extension. Journal of Petrology, 62, egab082.

Dong, J., Grove, M., Wei, C., Han, B.-F., Yin, A., Chen, J., Li, A., and Zhang, Z. (2022) Trench retreat recorded by a subduction zone metamorphic history. Geology, 50, 1281–1286.

Du, J.X., Zhang, L.F., Bader, T., Chen, Z.Y., and Lü, Z. (2014a) Metamorphic evolution of relict lawsonite-bearing eclogites from the (U)HP metamorphic belt in the Chinese southwestern Tianshan. Journal of Metamorphic Geology, 32, 575–598.

Du, J.-X., Zhang, L.-F., Shen, X.-J., and Bader, T. (2014b) A new *P-T-t* path of eclogites from Chinese southwestern Tianshan: constraints from *P-T* pseudosections and Sm-Nd isochron dating. Lithos, 200–201, 258–272.

Elburg, M.A., Foden, J.D., van Bergen, M.J., and Zulkarnain, I. (2005) Australia and Indonesia in collision: geochemical sources of magmatism. Journal of Volcanology and Geothermal Research, 140, 25–47.

Etheridge, M.A., Wall, V.J., Cox, S.F., and Vernon, R.H. (1984) High fluid pressures during regional metamorphism and deformation: Implications for mass transport and deformation mechanisms. Journal of Geophysical Research: Solid Earth, 89, 4344–4358.

Evans, B.W. (1990) Phase relations of epidote-blueschists. Lithos, 25, 3–23.

Ferrando, S., Petrelli, M., and Frezzotti, M.L. (2019) Gradual and selective trace-element enrichment in slab-released fluids at sub-arc depths. Scientific Reports, 9, 16393.

Gao, J., and Klemd, R. (2001) Primary fluids entrapped at blueschist to eclogite transition: evidence from the

Tianshan meta-subduction complex in northwestern China. Contributions to Mineralogy and Petrology, 142, 1–14.

Gao, J., and Klemd, R. (2003) Formation of HP–LT rocks and their tectonic implications in the western Tianshan Orogen, NW China: geochemical and age constraints. Lithos, 66, 1–22.

Gao, J., Li, M., Xiao, X., Tang, Y., and He, G. (1998) Paleozoic tectonic evolution of the Tianshan Orogen, northwestern China. Tectonophysics, 287, 213–231.

Gao, J., Klemd, R., Zhang, L., Wang, Z., and Xiao, X. (1999) P-T path of high-pressure/low-temperature rocks and tectonic implications in the western Tianshan Mountains, NW China. Journal of Metamorphic Geology, 17, 621–636.

Gao, J., John, T., Klemd, R., and Xiong, X. (2007) Mobilization of Ti–Nb–Ta during subduction: Evidence from rutile-bearing dehydration segregations and veins hosted in eclogite, Tianshan, NW China. Geochimica et Cosmochimica Acta, 71, 4974–4996.

Green, E., Holland, T., and Powell, R. (2007) An order-disorder model for omphacitic pyroxenes in the system jadeite-diopside-hedenbergite-acmite, with applications to eclogitic rocks. American Mineralogist, 92, 1181–1189.

Green, T.H., and Adam, J. (2003) Experimentally-determined trace element characteristics of aqueous fluid from partially dehydrated mafic oceanic crust at 3.0 GPa, 650-700°C. European Journal of Mineralogy, 15, 815–830.

Guo, S., Ye, K., Chen, Y., Liu, J., Mao, Q., and Ma, Y. (2012) Fluid–rock interaction and element mobilization in UHP metabasalt: Constraints from an omphacite–epidote vein and host eclogites in the Dabie orogen. Lithos, 136–139, 145–167.

Hacker, B.R., Peacock, S.M., Abers, G.A., and Holloway, S.D. (2003) Subduction factory 2. Are intermediate-depth earthquakes in subducting slabs linked to metamorphic dehydration reactions? Journal of Geophysical Research: Solid Earth, 108.

Hernández-Uribe, D., Hernández-Montenegro, J.D., Cone, K.A., and Palin, R.M. (2020) Oceanic slab-top melting during subduction: Implications for trace-element recycling and adakite petrogenesis. Geology, 48, 216–220.

Holland, T., and Powell, R. (2003) Activity-composition relations for phases in petrological calculations: an asymmetric multicomponent formulation. Contributions to Mineralogy and Petrology, 145, 492–501.

Holland, T., Baker, J., and Powell, R. (1998) Mixing properties and activity-composition relationships of chlorites in the system MgO-FeO-Al_2O_3-SiO_2-H_2O. European Journal of Mineralogy, 10, 395–406.

Holland, T.J.B., and Powell, R. (1998) An internally consistent thermodynamic data set for phases of petrological interest. Journal of Metamorphic Geology, 16, 309–343.

Ikemoto, A., and Iwamori, H. (2014) Numerical modeling of trace element transportation in subduction zones: implications for geofluid processes. Earth, Planets and Space, 66, 26.

John, T., Klemd, R., Gao, J., and Garbe-Schönberg, C.-D. (2008) Trace-element mobilization in slabs due to non steady-state fluid–rock interaction: Constraints from an eclogite-facies transport vein in blueschist (Tianshan, China). Lithos, 103, 1–24.

John, T., Gussone, N., Podladchikov, Y.Y., Bebout, G.E., Dohmen, R., Halama, R., Klemd, R., Magna, T., and Seitz, H.-M. (2012) Volcanic arcs fed by rapid pulsed fluid flow through subducting slabs. Nature Geoscience, 5, 489–492.

Jung, H., Green II, H.W., and Dobrzhinetskaya, L.F. (2004) Intermediate-depth earthquake faulting by dehydration embrittlement with negative volume change. Nature, 428, 545–549.

Kessel, R., Schmidt, M.W., Ulmer, P., and Pettke, T. (2005) Trace element signature of subduction-zone fluids, melts and supercritical liquids at 120–180 km depth. Nature, 437, 724–727.

Klemd, R., Gao, J., Li, J.-L., and Meyer, M. (2015) Metamorphic evolution of (ultra)-high-pressure subduction-related transient crust in the South Tianshan Orogen (Central Asian Orogenic Belt): Geodynamic implications. Gondwana Research, 28, 1–25.

Lan, C., Tao, R., Huang, F., Jiang, R., and Zhang, L. (2023) High-pressure experimental and thermodynamic constraints on the solubility of carbonates in subduction zone fluids. Earth and Planetary Science Letters, 603, 117989.

Leake, B.E., Woolley, A.R., Arps, C.E.S., Birch, W.D., Gilbert, M.C., Grice, J.D., Hawthorne, F.C., Kato, A., Kisch, H.J., Krivovichev, V.G., and others (1997) Nomenclature of Amphiboles: Report of the Subcommittee on Amphiboles of the International Mineralogical Association Commission on New Minerals and Mineral Names. Mineralogical Magazine, 61, 295–321.

Li, H., Hermann, J., and Zhang, L. (2022) Melting of subducted slab dictates trace element recycling in global arcs. Science Advances, 8, eabh2166.

Li, J.-L., Gao, J., John, T., Klemd, R., and Su, W. (2013) Fluid-mediated metal transport in subduction zones and its link to arc-related giant ore deposits: Constraints from a sulfide-bearing HP vein in lawsonite eclogite (Tianshan, China). Geochimica et Cosmochimica Acta, 120, 326–362.

Li, J.-L., John, T., Gao, J., Klemd, R., and Wang, X.-S. (2017a) Subduction channel fluid–rock interaction and mass transfer: Constraints from a retrograde vein in blueschist (SW Tianshan, China). Chemical Geology, 456, 28–42.

Li, J.-L., Schwarzenbach, E.M., John, T., Ague, J.J., Huang, F., Gao, J., Klemd, R., Whitehouse, M.J., and Wang, X.-S. (2020) Uncovering and quantifying the subduction zone sulfur cycle from the slab perspective. Nature Communications, 11, 12.

Li, J.-L., Schwarzenbach, E.M., John, T., Ague, J.J., Tassara, S., Gao, J., and Konecke, B.A. (2021) Subduction zone sulfur mobilization and redistribution by intraslab fluid–rock interaction. Geochimica et Cosmochimica Acta, 297, 40–64.

Li, S.-G., Yang, W., Ke, S., Meng, X., Tian, H., Xu, L., He, Y., Huang, J., Wang, X.-C., Xia, Q., and others (2017b) Deep carbon cycles constrained by a large-scale mantle Mg isotope anomaly in eastern China. National Science Review, 4, 111–120.

Liu, Y., Hu, Z., Gao, S., Günther, D., Xu, J., Gao, C., and Chen, H. (2008) In situ analysis of major and trace elements of anhydrous minerals by LA-ICP-MS without applying an internal standard. Chemical Geology, 257, 34–43.

Lü, Z., Zhang, L., Du, J., and Bucher, K. (2009) Petrology of coesite-bearing eclogite from Habutengsu Valley, western Tianshan, NW China and its tectonometamorphic implication. Journal of Metamorphic Geology, 27, 773–787.

Lü, Z., Zhang, L., Du, J., Yang, X., Tian, Z., and Xia, B. (2012a) Petrology of HP metamorphic veins in coesite-bearing eclogite from western Tianshan, China: Fluid processes and elemental mobility during exhumation in a cold subduction zone. Lithos, 136–139, 168–186.

Lü, Z., Bucher, K., Zhang, L., and Du, J. (2012b) The Habutengsu metapelites and metagreywackes in western Tianshan, China: metamorphic evolution and tectonic implications. Journal of Metamorphic Geology, 30, 907–926.

Martin, L.A.J., Wood, B.J., Turner, S., and Rushmer, T. (2011) Experimental measurements of trace element partitioning between lawsonite, zoisite and fluid and their implication for the composition of arc magmas. Journal of Petrology, 52, 1049–1075.

Martin, L.A.J., Hermann, J., Gauthiez-Putallaz, L., Whitney, D.L., Vitale Brovarone, A., Fornash, K.F., and

Evans, N.J. (2014) Lawsonite geochemistry and stability - implication for trace element and water cycles in subduction zones. Journal of Metamorphic Geology, 32, 455–478.

Molina, J.F., and Poli, S. (2000) Carbonate stability and £uid composition in subducted oceanic crust: an experimental study on H2O^CO2-bearing basalts. Earth and Planetary Science Letters, 176, 295–310.

Morimoto, N., Fabries, J., Ferguson, A.K., Ginzburg, I.V., Ross, M., Seifert, F.A., Zussman, J., Aoki, K., and Gottardi, G. (1989) Nomenclature of pyroxenes. Mineralogical Journal, 14, 198–221.

Orozbaev, R., Hirajima, T., Bakirov, Apas, Takasu, A., Maki, K., Yoshida, K., Sakiev, K., Bakirov, Azamat, Hirata, T., Tagiri, M., and others (2015) Trace element characteristics of clinozoisite pseudomorphs after lawsonite in talc-garnet-chloritoid schists from the Makbal UHP Complex, northern Kyrgyz Tian-Shan. Lithos, 226, 98–115.

Philippot, P., and Selverstone, J. (1991) Trace-element-rich brines in eclogitic veins: implications for fluid composition and transport during subduction. Contributions to Mineralogy and Petrology, 106, 417–430.

Pirard, C., and Hermann, J. (2015) Focused fluid transfer through the mantle above subduction zones. Geology, 43, 915–918.

Sokol, A.G., Kozmenko, O.A., and Kruk, A.N. (2023) Composition of supercritical fluid in carbonate- and chlorine-bearing pelite at conditions of subduction zones. Contributions to Mineralogy and Petrology, 178, 90.

Spandler, C., and Pirard, C. (2013) Element recycling from subducting slabs to arc crust: A review. Lithos, 170–171, 208–223.

Spandler, C., Hermann, J., Arculus, R., and Mavrogenes, J. (2003) Redistribution of trace elements during prograde metamorphism from lawsonite blueschist to eclogite facies; implications for deep subduction-zone processes. Contributions to Mineralogy and Petrology, 146, 205–222.

Spandler, C., Mavrogenes, J., and Hermann, J. (2007) Experimental constraints on element mobility from subducted sediments using high-P synthetic fluid/melt inclusions. Chemical Geology, 22.

Spandler, C., Pettke, T., and Rubatto, D. (2011) Internal and external fluid sources for eclogite-facies veins in the Monviso meta-ophiolite, western Alps: Implications for fluid flow in subduction zones. Journal of Petrology, 52, 1207–1236.

Spear, F.S. (1995) Metamorphic Phase Equilibria and Pressure-Temperature-Time Paths Monograph Series, 799 pp. p. Mineralogical Society of America Monograph 2nd Vol. 5. Washington, DC.

Sun, S. -s., and McDonough, W.F. (1989) Chemical and isotopic systematics of oceanic basalts: implications for mantle composition and processes. Geological Society, London, Special Publications, 42, 313–345.

Tagiri, M., Yano, T., Bakirov, A., Nakajima, T., and Uchiumi, S. (1995) Mineral parageneses and metamorphic P-T paths of ultrahigh-pressure eclogites from Kyrghyzstan Tien-Shan. The Island Arc, 4, 280–292.

Tan, Z., Agard, P., Gao, J., John, T., Li, J., Jiang, T., Bayet, L., Wang, X., and Zhang, X. (2017) P–T–time-isotopic evolution of coesite-bearing eclogites: Implications for exhumation processes in SW Tianshan. Lithos, 278–281, 1–25.

Tan, Z., Agard, P., Monié, P., Gao, J., John, T., Bayet, L., Jiang, T., Wang, X.-S., Hong, T., Wan, B., and others (2019) Architecture and P-T-deformation-time evolution of the Chinese SW-Tianshan HP/UHP complex: Implications for subduction dynamics. Earth-Science Reviews, 197, 102894.

Tang, P., Guo, S., Yang, Y., Chen, Y., and Su, B. (2021) Evolution of fluids and melts in deeply subducted continental crust: Insights from an UHP eclogite–vein system in the Dabie terrane, China. Lithos, 398–399, 106325.

Teng, F.-Z., Hu, Y., and Chauvel, C. (2016) Magnesium isotope geochemistry in arc volcanism. Proceedings of the National Academy of Sciences, 113, 7082–7087.

Tian, Z.L., and Wei, C.J. (2014) Coexistence of garnet blueschist and eclogite in South Tianshan, NW China: dependence of *P-T* evolution and bulk-rock composition. Journal of Metamorphic Geology, 32, 743–764.

Tsay, A., Zajacz, Z., and Sanchez-Valle, C. (2014) Efficient mobilization and fractionation of rare-earth elements by aqueous fluids upon slab dehydration. Earth and Planetary Science Letters, 398, 101–112.

Tsay, A., Zajacz, Z., Ulmer, P., and Sanchez-Valle, C. (2017) Mobility of major and trace elements in the eclogite-fluid system and element fluxes upon slab dehydration. Geochimica et Cosmochimica Acta, 198, 70–91.

Tsujimori, T., and Ernst, W.G. (2014) Lawsonite blueschists and lawsonite eclogites as proxies for palaeo-subduction zone processes: a review. Journal of Metamorphic Geology, 32, 437–454.

Turner, S., and Foden, J. (2001) U, Th and Ra disequilibria, Sr, Nd and Pb isotope and trace element variations in Sunda arc lavas: Predominance of a subducted sediment component. Contributions to Mineralogy and Petrology, 142, 43–57.

van der Straaten, F., Schenk, V., John, T., and Gao, J. (2008) Blueschist-facies rehydration of eclogites (Tian Shan, NW-China): Implications for fluid–rock interaction in the subduction channel. Chemical Geology, 255, 195–219.

van der Straaten, F., Halama, R., John, T., Schenk, V., Hauff, F., and Andersen, N. (2012) Tracing the effects of high-pressure metasomatic fluids and seawater alteration in blueschist-facies overprinted eclogites: Implications for subduction channel processes. Chemical Geology, 292–293, 69–87.

Volkova, N.I., and Budanov, V.I. (1999) Geochemical discrimination of metabasalt rocks of the Fan–Karategin transitional blueschist/greenschist belt, South Tianshan, Tajikistan: seamount volcanism and accretionary tectonics. Lithos, 47, 201–216.

Vry, J., Powell, R., Golden, K.M., and Petersen, K. (2010) The role of exhumation in metamorphic dehydration and fluid production. Nature Geoscience, 3, 31–35.

Wang, S.-J., Teng, F.-Z., Li, S.-G., Zhang, L.-F., Du, J.-X., He, Y.-S., and Niu, Y. (2017) Tracing subduction zone fluid-rock interactions using trace element and Mg-Sr-Nd isotopes. Lithos, 290–291, 94–103.

Wang, Y., Zhang, L., Li, Z., Li, Q., and Bader, T. (2019) The exhumation of subducted oceanic-derived eclogites: Insights from phase equilibrium and thermomechanical modeling. Tectonics, 38, 1764–1797.

White, A.J.R., Waters, D.J., and Robb, L.J. (2015) Exhumation-Driven Devolatilization as a Fluid Source for Orogenic Gold Mineralization at the Damang Deposit, Ghana. Economic Geology, 110, 1009–1025.

White, R.W., Pomroy, N.E., and Powell, R. (2005) An in situ metatexite-diatexite transition in upper amphibolite facies rocks from Broken Hill, Australia. Journal of Metamorphic Geology, 23, 579–602.

Whitney, D.L., and Evans, B.W. (2010) Abbreviations for names of rock-forming minerals. American Mineralogist, 95, 185–187.

Wu, S., and Xiao, Y. (2023) Various fluids and complex geochemical processes in the subduction channel: Constraints from the ultrahigh pressure metamorphic belt of Southwestern Tianshan, China. Lithos, 442–443, 107077.

Xia, B., Shang, Y., Lu, X., and Wu, Y. (2023) UHP eclogite from western Dabie records evidence of polycyclic burial during continental subduction. American Mineralogist, 108, 1330–1345.

Yang, X., Zhang, L., Tian, Z., and Bader, T. (2013) Petrology and U–Pb zircon dating of coesite-bearing metapelite from the Kebuerte Valley, western Tianshan, China. Journal of Asian Earth Sciences, 70–71, 295–307.

Zack, T., and John, T. (2007) An evaluation of reactive fluid flow and trace element mobility in subducting slabs. Chemical Geology, 239, 199–216.

Zhang, L., and Wang, Y. (2020) The exhumation of high- and ultrahigh-pressure metamorphic terranes in subduction zone: Questions and discussions. Science China Earth Sciences, 63.

Zhang, L., Gao, J., Ekebair, S., and Wang, Z. (2001) Low temperature eclogite facies metamorphism in Western Tianshan, Xinjiang. Science in China Series D: Earth Sciences, 44, 85–96.

Zhang, L., Ellis, D.J., Williams, S., and Jiang, W. (2002a) Ultra-high pressure metamorphism in western Tianshan, China: Part II. Evidence from magnesite in eclogite. American Mineralogist, 87, 861–866.

Zhang, L., Ellis, D.J., and Jiang, W. (2002b) Ultrahigh-pressure metamorphism in western Tianshan, China: Part I. Evidence from inclusions of coesite pseudomorphs in garnet and from quartz exsolution lamellae in omphacite in eclogites. American Mineralogist, 87, 853–860.

Zhang, L., Ai, Y., Song, S., Liou, J., and Wei, C. (2007) A brief review of UHP meta-ophiolitic rocks, southwestern Tianshan, western China. International Geology Review, 49, 811–823.

Zhang, L., Lü, Z., Zhang, G., and Song, S. (2008) The geological characteristics of oceanic-type UHP metamorphic belts and their tectonic implications: Case studies from Southwest Tianshan and North Qaidam in NW China. Science Bulletin, 53, 3120–3130.

Zhang, Lifei, Wang, Y., Zhang, Lijuan, and Lü, Z. (2019) Ultrahigh pressure metamorphism and tectonic evolution of southwestern Tianshan orogenic belt, China: a comprehensive review. Geological Society, London, Special Publications, 474, 133–152.

Zhang, Lijuan, Zhang, Lifei, Lü, Z., Bader, T., and Chen, Z. (2016) Nb–Ta mobility and fractionation during exhumation of UHP eclogite from southwestern Tianshan, China. Journal of Asian Earth Sciences, 122, 136–157.

Zheng, Y., Chen, R., Xu, Z., and Zhang, S. (2016) The transport of water in subduction zones. Science China Earth Sciences, 59, 651–682.

Zheng, Y.-F. (2019) Subduction zone geochemistry. Geoscience Frontiers, 10, 1223–1254.

Zhu, J., Zhang, L., Tao, R., and Fei, Y. (2020) The formation of graphite-rich eclogite vein in S.W. Tianshan (China) and its implication for deep carbon cycling in subduction zone. Chemical Geology, 533, 119430.

Figure Captions

FIGURE 1. Geological map of (U)HP metamorphic belt in Chinese southwestern Tianshan (modified after Tan et al. 2017). (**a**) Regional tectonic map, and (**b**) close-up geological map showing sample location.

FIGURE 2. Photographs of the host eclogite and the embedded omphacite-rich vein in Chinese Southwest Tianshan. (**a**) A polished hand specimen of the eclogite-vein system (sample A300-12). (**b**) Photomicrograph of the thin section showing the omphacite-rich vein and the host eclogite. (**c**) Photomicrograph of the area indicated in (**b**) showing mineral assemblages of the vein and contact boundary between the host eclogite and the vein. (**d**) Photomicrograph of the area indicated in **(b)** showing the host eclogite mineral assemblages. Back scattered electron (BSE) images showing that (**e**) harbor-shaped garnet rim was filled with matrix phengite of the host eclogite, (**f**) aegirine-augite and omphacite occurrences in the host eclogite, (**g**) epidote + paragonite inclusions in host garnet, (**h**) rutile inclusions in epidote and the matrix rutile replaced by titanite in the host eclogite, (**i**) omphacite zoning pattern in the vein, and **(j)** different clinopyroxene inclusions within garnet growing at the eclogite-vein wall ($Grt_{V\text{-}E}$).

FIGURE 3. TIMA images showing (**a**) almost no inclusion in core of garnet in the vein, (**b**) different inclusion characteristics of the garnet core between the host eclogite and the vein, and (**c**) a few inclusions in the garnet rim of the host eclogite.

FIGURE 4. Chemical compositions of garnet, clinopyroxene, glaucophane, and epidote. (**a**) Ternary diagram of garnet Alm+Sps (Almandine + Spessartite) -Grs (grossular) -Prp (pyrope). The V-side in $Grt_{V\text{-}E}$ and E-side in $Grt_{V\text{-}E}$ represent $Grt_{V\text{-}E}$ on the side of the vein and the host eclogite, respectively. (**b**) Compositional triangle for clinopyroxene classification after Morimoto (1989), represented by WEF (wollite + enstatiopyrene + ferroopyrene) -Jd (jadeite) -Aeg (aegirine). Quad = Ca-Mg-Fe pyroxene. (**c** and **d**) Chemical compositions of

glaucophane and epidote.

FIGURE 5. Representative photomicrographs, TIMA images, and compositional profiles of (**a**–**c**) Grt_V, (**d**–**f**) $Grt_{V\text{-}E}$; (**g**–**i**) Grt_E. Red arrows in (**a**), (**d**) and (**g**) indicate the analysis position for zoning profiles, whereas dashed yellow line in (**d**) represents the boundary between the host eclogite and the omphacite-rich vein.

FIGURE 6. Representative chondrite-normalized REE patterns of (**a** and **b**) Grt_E, (**c**) Grt_V, (**d**) $Grt_{V\text{-}E}$, (**e**) epidote and allanite, (**f**) apatite of the host eclogite and vein. Normalization values are from Sun and McDonough (1989). The V-side in $Grt_{V\text{-}E}$ and E-side in $Grt_{V\text{-}E}$ represent $Grt_{V\text{-}E}$ on the side of the vein and the host eclogite, respectively. Red arrows indicate the analysis position and direction of the laser point, whereas dashed gray line in (**d**) represents the boundary between the host eclogite and the omphacite-rich vein.

FIGURE 7. Primitive mantle-normalized trace element spider diagrams of (**a**) epidote and allanite of the host eclogite and vein and (**b**) apatite of the vein. Normalization values are from Sun and McDonough (1989).

FIGURE 8. (**a**) P-T pseudosection for the host eclogite in the system MnNCKFASCHOTi calculated with an effective bulk composition. The pseudosections are contoured with (**b**) grossular (purple), pyrope (orange) isopleths in garnet and Si isopleths in phengite (p.f.u., yellow) and (**c**) H_2O isopleths in solid phases (mol.%). (**d**–**f**) Calculated volume percentage of mainly hydrous minerals chlorite, lawsonite and glaucophane (vol.%). The circles with colors from yellow to red point to garnet compositions from core to rim in the host eclogite, and the dotted gray line with arrows from A to D represents the inferred P-T path. Red arrows denote geothermal gradients.

FIGURE 9. Computed modal variations of the major minerals and water content in solid phases along the P-T path shown in Fig. 8a. The colored solid lines represent the mineral modal amounts and the gray areas represent the water contents (mol.%). The dotted line represents P-T conditions recorded by garnet inner core.

FIGURE 10. Schematic diagram illustrating the formation of the studied eclogite-vein system during the

metamorphic evolution of subduction-exhumation processes. S1–S7 represents petrological characteristics of the eclogite-vein system at different stages on the P-T path. The pink domain represents the host eclogite and the blue domain represents the vein.

FIGURE 11. Representative trace element concentrations of multi-stage vein-forming fluids calculated by mineral-fluid coefficients. Stages 1–3 represent fluid compositions in equilibrium with core of garnet, omphacite + mantle/rim of garnet and epidote in the vein, respectively. Heavy lines with arrows indicate potential evolutionary trends for fluids.

FIGURE 12. Primitive mantle-normalized diagram of the calculated fluid compositions at each stage in the studied omphacite-rich vein. Average fluid compositions calculated from core of garnet (stage 1), mantle/rim of garnet (stage 2), omphacite (stage 2) and epidote (stage 3) are shown as blue, green, yellow and red points, respectively. The gray field and purple line denote the compositions of continental and island arc basalts and N-MORB, respectively. The range of continental and island arc basalts are from Borg et al. (2000), Turner and Foden (2001), Elburg et al. (2005), Teng et al. (2016), Li et al. (2017b) and data compiled by GEOROC (https://georoc.eu/). The primitive mantle normalization values and the average compositions for N-MORB are from Sun and McDonough (1989).

FIGURE 13. (a) Schematic diagram for dehydration of oceanic crust and melting of mantle wedge during subduction and exhumation. (b) Detailed schematic diagram showing subduction and exhumation of the eclogite and associated fluid behavior. Blue arrows represent dehydration of subducting oceanic crust. Dashed green arrows represent potential subduction and exhumation path for the eclogite. Pink arrows represent solutes released by the eclogite during dehydration. A-D corresponds to that in Fig. 8a. Stages 1-3 correspond to those in Fig. 11.

This is the peer-reviewed, final accepted version for American Mineralogist, published by the Mineralogical Society of America.
The published version is subject to change. Cite as Authors (Year) Title. American Mineralogist, in press.
DOI: https://doi.org/10.2138/am-2023-9218. http://www.minsocam.org/

Supporting information

Table S1. Major element compositions of representative minerals in the eclogite and the vein from Chinese southwestern Tianshan.

Table S2. Trace element compositions of representative minerals in the eclogite and the vein from Chinese southwestern Tianshan.

Figure S1. (**a**) Calculated volume percentage of garnet (vol.%) for the host eclogite; (**b**) the effect of clinopyroxene fractionation and non-fractionation on its Al/(Al+Fe^{3+}) along the assumed P-T path. Dashed line with arrow represents the P-T path from Fig. 8a.

Figure S2. Trace element concentrations of multi-stage vein-forming fluids calculated by mineral-fluid coefficients. Stages 1–3 represents fluid compositions in equilibrium with core of garnet, omphacite + mantle/rim of garnet and epidote in the vein, respectively. Heavy lines with arrows indicate potential evolutionary trends for fluids. Shown here are elements other than those in Fig. 11.

This is the peer-reviewed, final accepted version for American Mineralogist, published by the Mineralogical Society of America.
The published version is subject to change. Cite as Authors (Year) Title. American Mineralogist, in press.
DOI: https://doi.org/10.2138/am-2023-9218. http://www.minsocam.org/

Figure 1

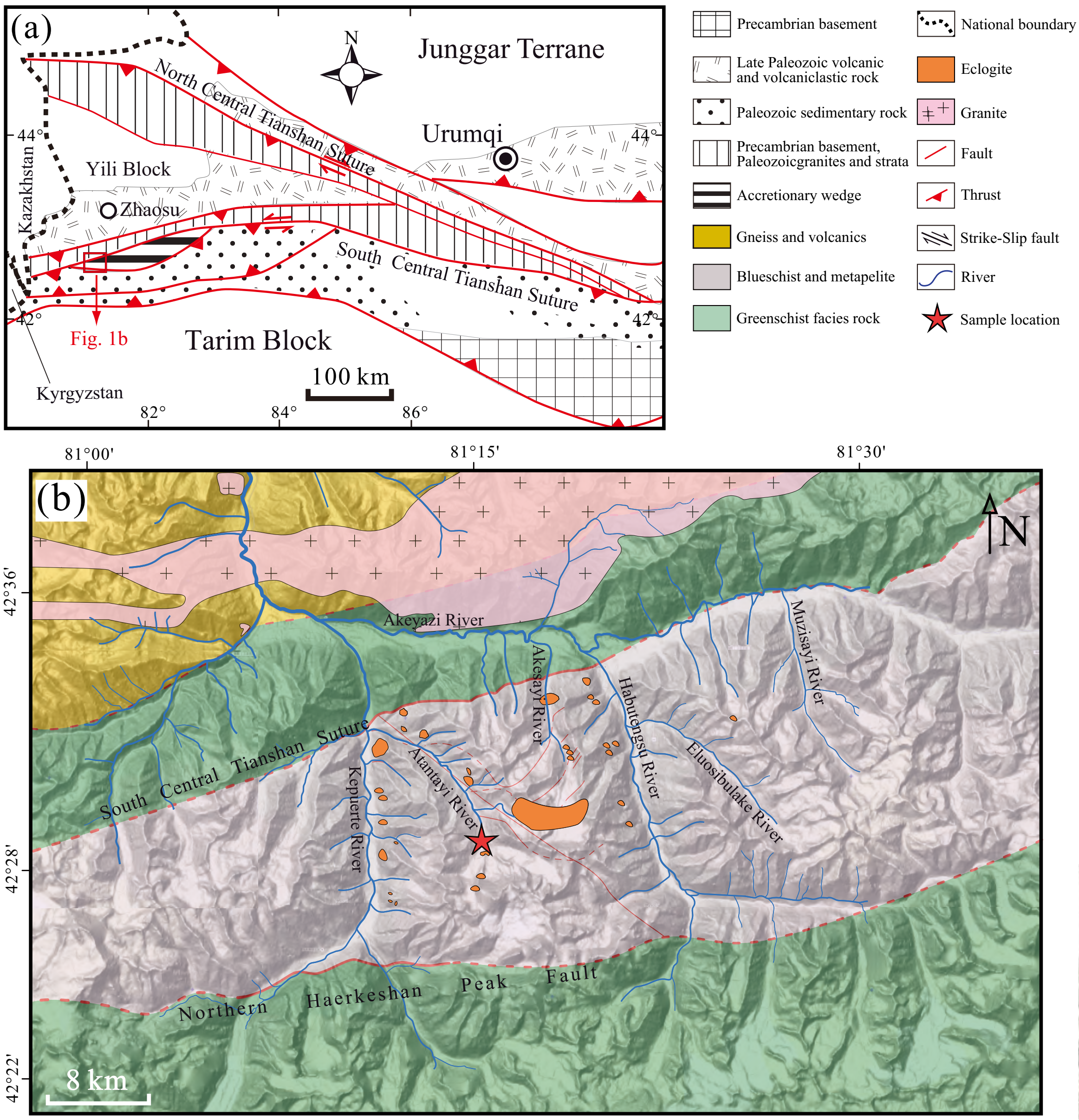

This is the peer-reviewed, final accepted version for American Mineralogist, published by the Mineralogical Society of America.
The published version is subject to change. Cite as Authors (Year) Title. American Mineralogist, in press.
DOI: https://doi.org/10.2138/am-2023-9218. http://www.minsocam.org/

Figure 2

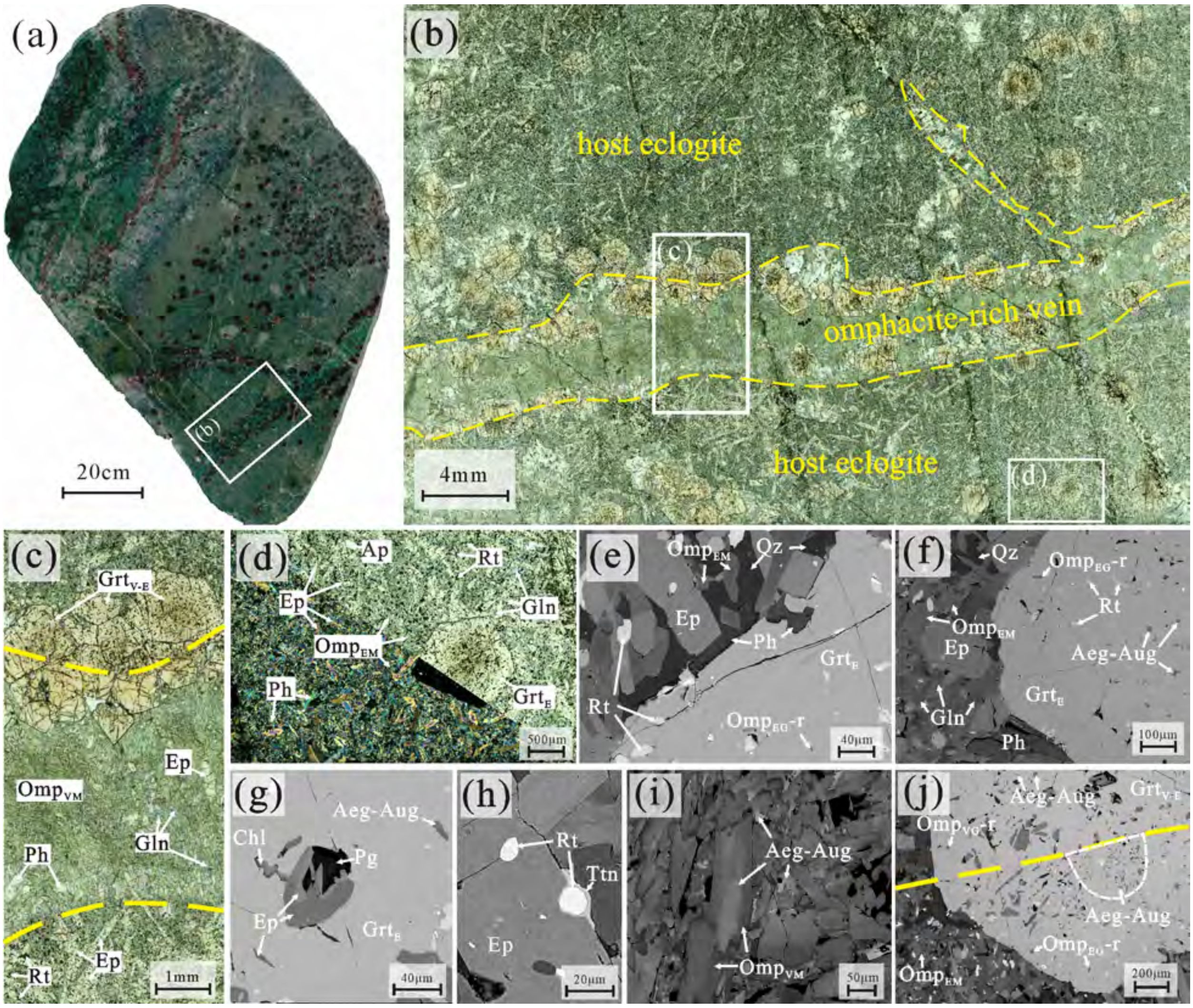

This is the peer-reviewed, final accepted version for American Mineralogist, published by the Mineralogical Society of America.
The published version is subject to change. Cite as Authors (Year) Title. American Mineralogist, in press.
DOI: https://doi.org/10.2138/am-2023-9218. http://www.minsocam.org/

Figure 3

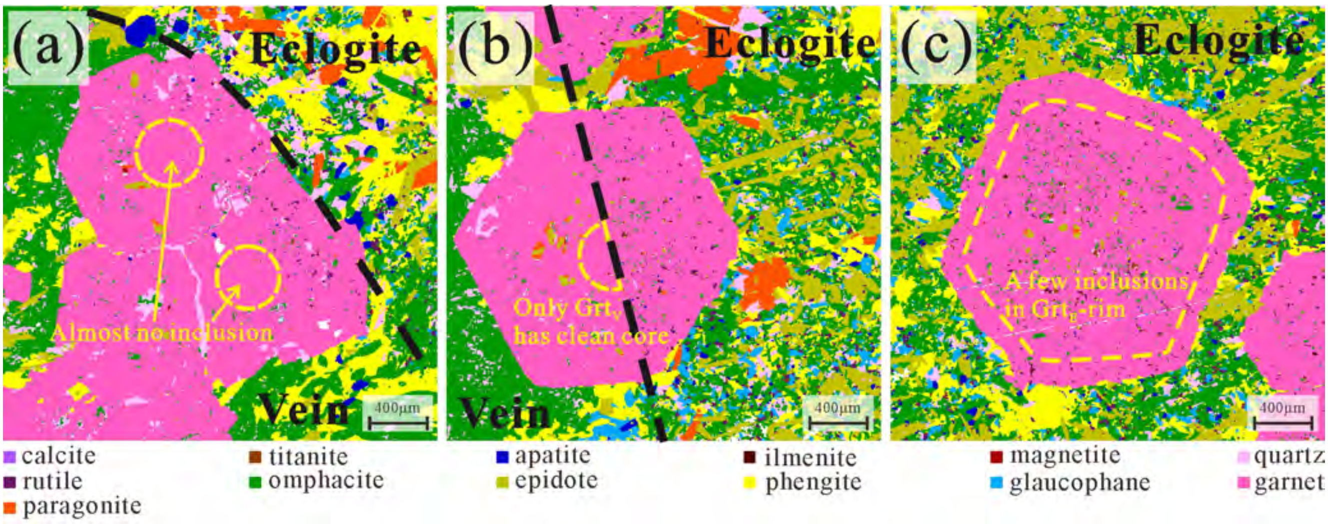

This is the peer-reviewed, final accepted version for American Mineralogist, published by the Mineralogical Society of America.
The published version is subject to change. Cite as Authors (Year) Title. American Mineralogist, in press.
DOI: https://doi.org/10.2138/am-2023-9218. http://www.minsocam.org/

Figure 4

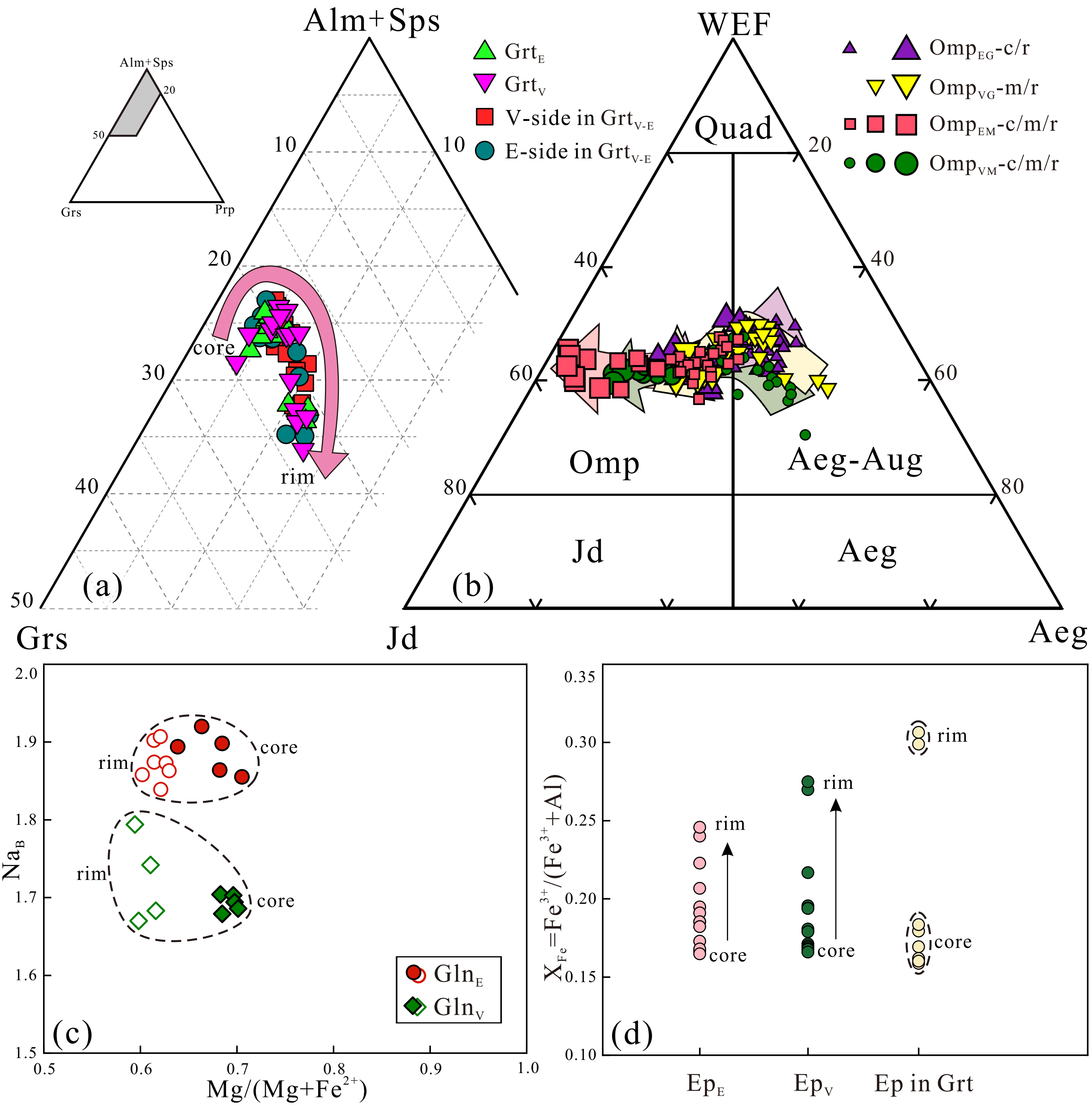

Figure 5

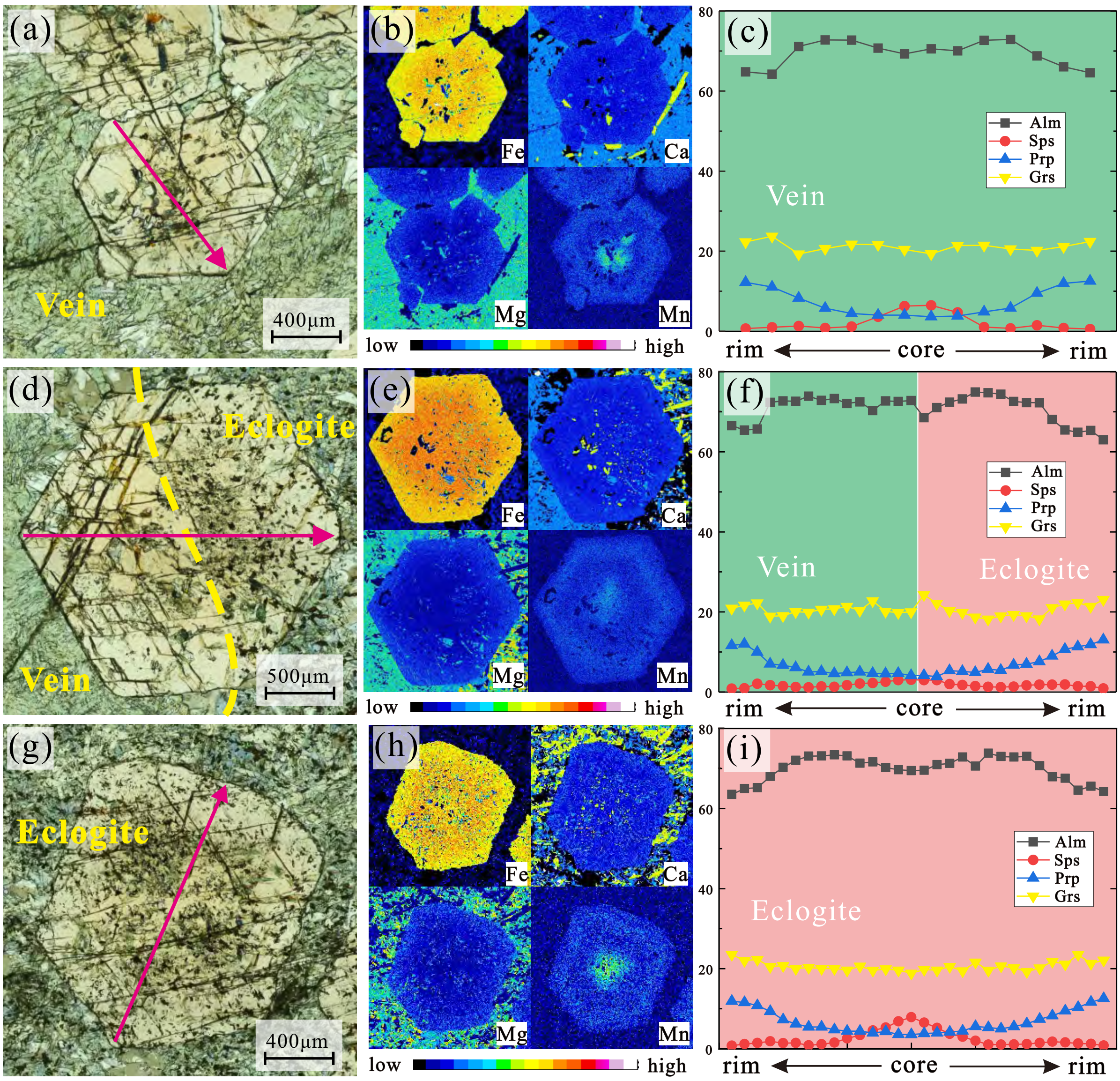
(a)
Vein
400μm
(b)
Fe
Ca
Mg
Mn
low
high
(c)
80
60
40
20
0
Alm
Sps
Prp
Grs
Vein
rim
core
rim
(d)
Eclogite
Vein
500μm
(e)
Fe
Ca
Mg
Mn
low
high
(f)
Alm
Sps
Prp
Grs
Vein
Eclogite
rim
core
rim
(g)
Eclogite
400μm
(h)
Fe
Ca
Mg
Mn
low
high
(i)
Alm
Sps
Prp
Grs
Eclogite
rim
core
rim

This is the peer-reviewed, final accepted version for American Mineralogist, published by the Mineralogical Society of America.
The published version is subject to change. Cite as Authors (Year) Title. American Mineralogist, in press.
DOI: https://doi.org/10.2138/am-2023-9218. http://www.minsocam.org/

Figure 6

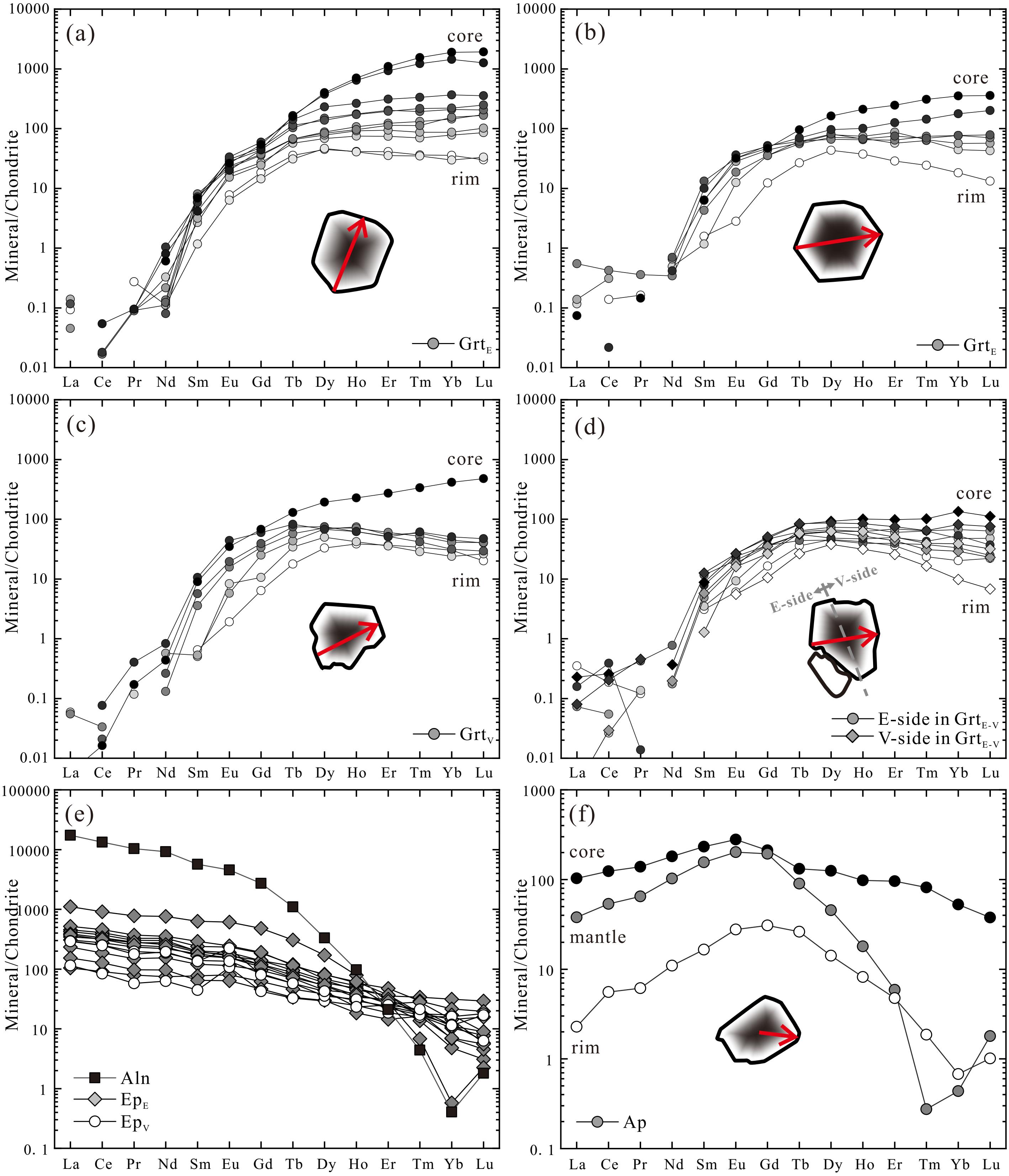

Figure 7

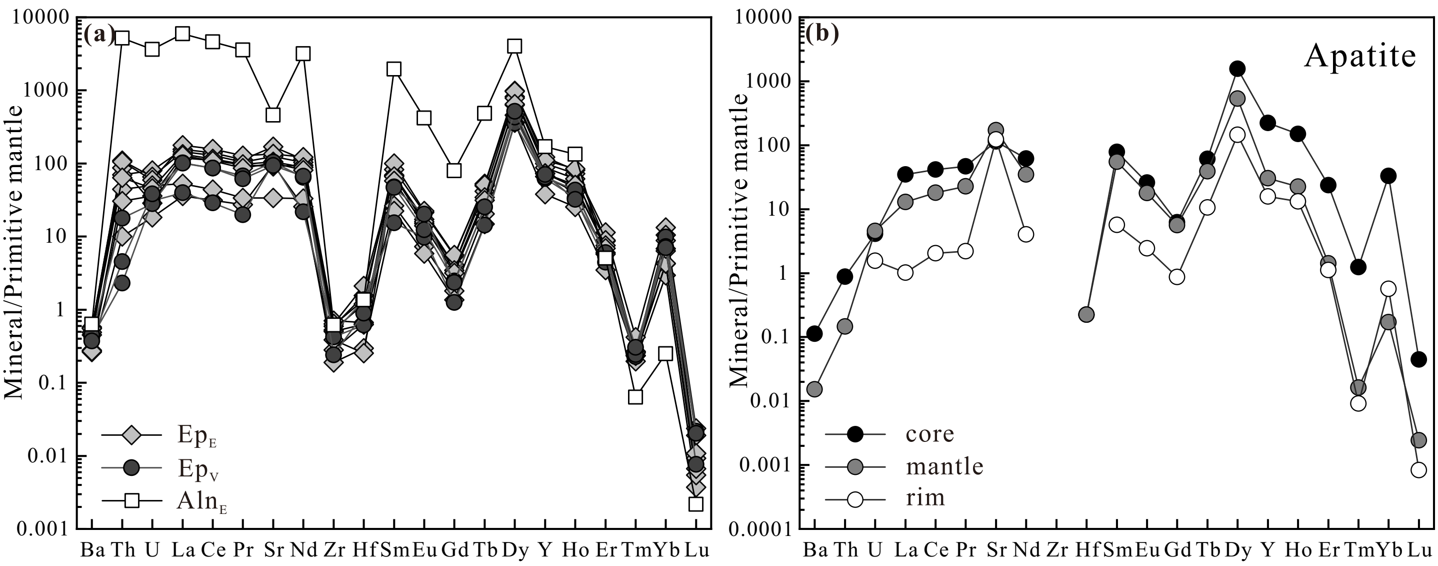
(a)
Mineral/Primitive mantle
10000
1000
100
10
1
0.1
0.01
0.001
Ep$_E$
Ep$_V$
Aln$_E$
Ba Th U La Ce Pr Sr Nd Zr Hf Sm Eu Gd Tb Dy Y Ho Er Tm Yb Lu
(b)
Apatite
Mineral/Primitive mantle
10000
1000
100
10
1
0.1
0.01
0.001
0.0001
core
mantle
rim
Ba Th U La Ce Pr Sr Nd Zr Hf Sm Eu Gd Tb Dy Y Ho Er Tm Yb Lu

Figure 8

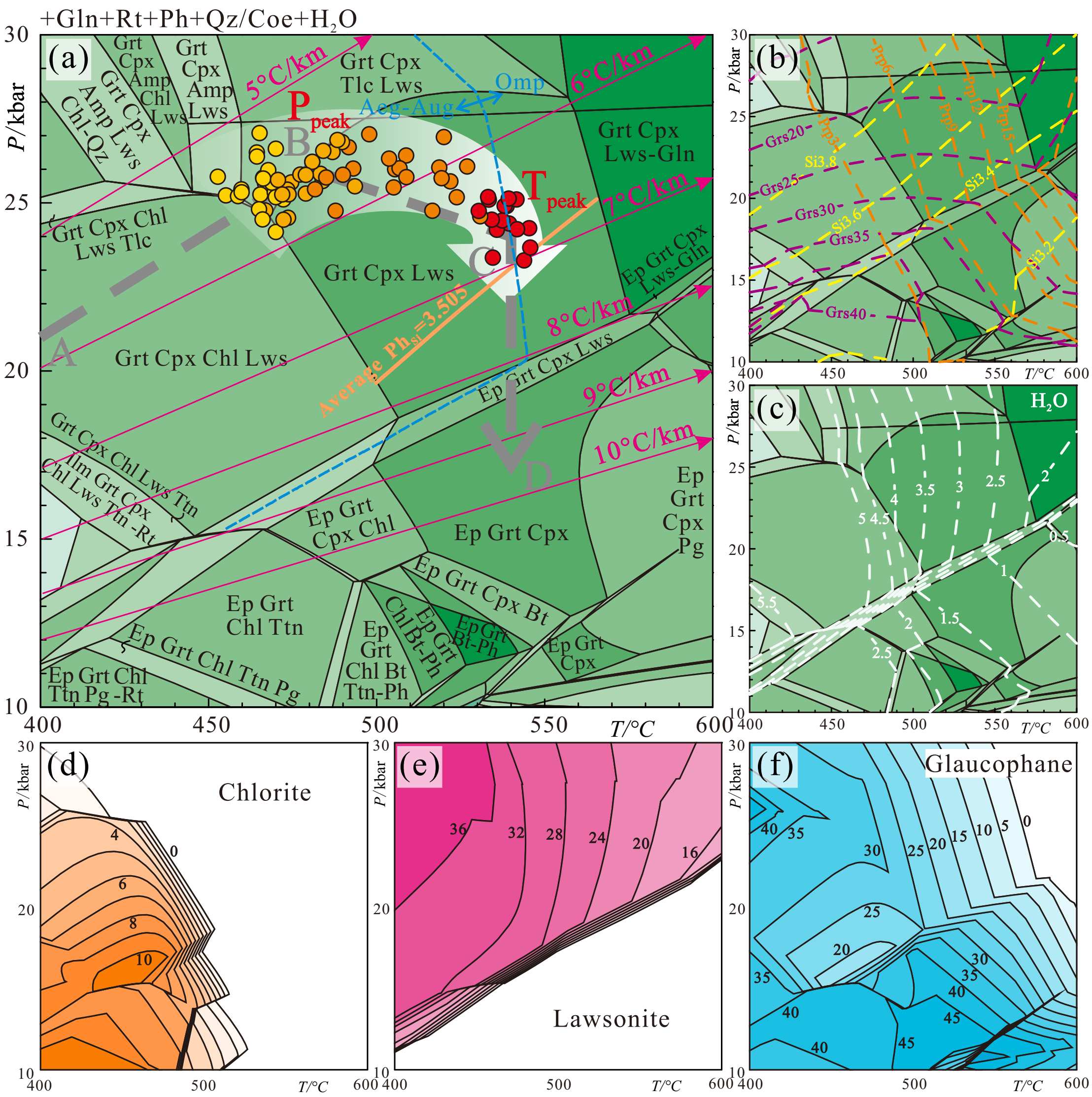
+Gln+Rt+Ph+Qz/Coe+H2O
(a)
P/kbar
T/°C
5°C/km
6°C/km
7°C/km
8°C/km
9°C/km
10°C/km
Ppeak
Tpeak
Omp
Aeg-Aug
Average Ph_Si=3.505
Grt Cpx Tlc Lws
Grt Cpx Lws-Gln
Grt Cpx Chl Lws Tlc
Grt Cpx Lws
Grt Cpx Chl Lws
Ep Grt Cpx Lws
Ep Grt Cpx Chl
Ep Grt Cpx
Ep Grt Chl Ttn
Ep Grt Chl Ttn Pg
Ep Grt Chl Ttn Pg -Rt
Ep Grt Cpx Bt
Ep Grt Cpx Pg
(b)
(c)
H2O
(d)
Chlorite
(e)
Lawsonite
(f)
Glaucophane

Figure 9

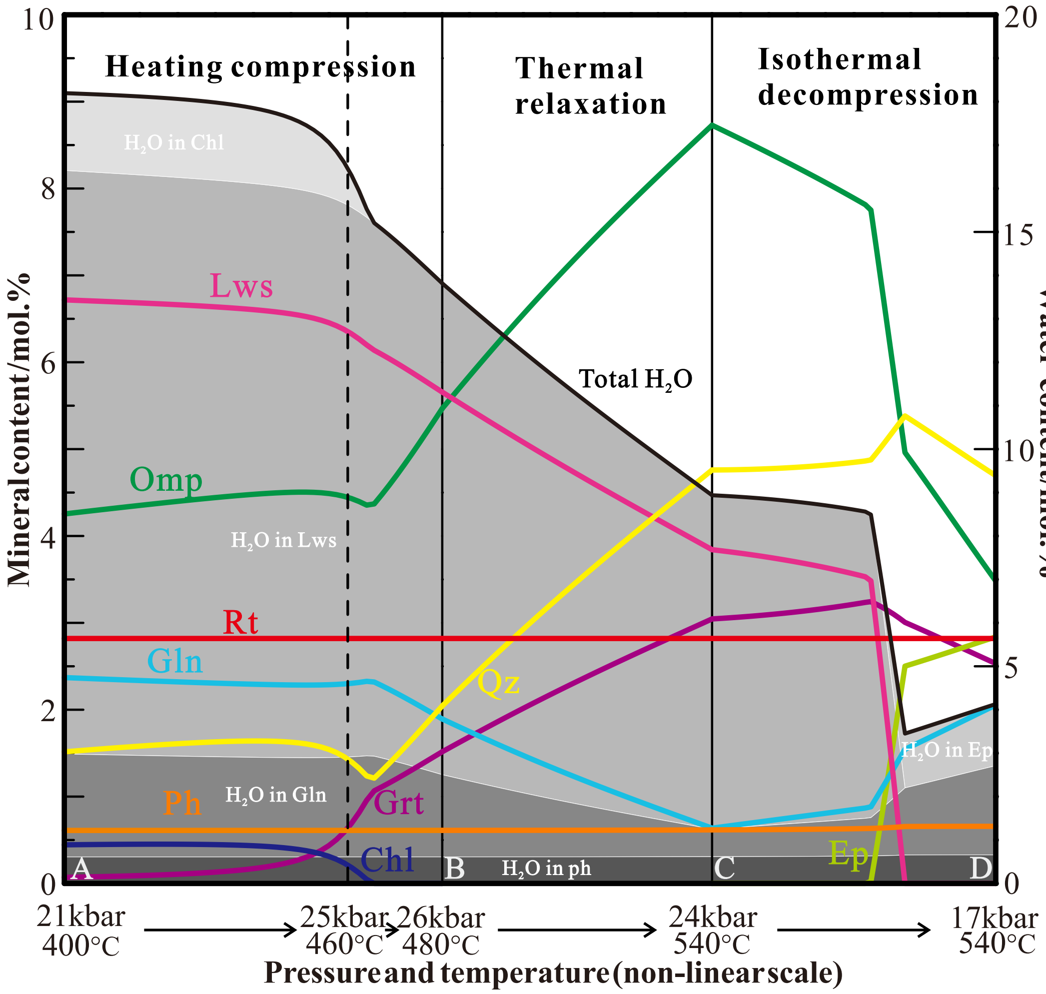
Heating compression
Thermal relaxation
Isothermal decompression
H2O in Chl
Lws
Total H2O
Omp
H2O in Lws
Rt
Gln
Qz
Grt
Ph
H2O in Gln
H2O in Ep
Chl
Ep
A
B
H2O in ph
C
D
Mineral content/mol.%
Water content/mol.%
10
8
6
4
2
0
20
15
10
5
0
21kbar 400°C
25kbar 460°C
26kbar 480°C
24kbar 540°C
17kbar 540°C
Pressure and temperature (non-linear scale)

This is the peer-reviewed, final accepted version for American Mineralogist, published by the Mineralogical Society of America.
The published version is subject to change. Cite as Authors (Year) Title. American Mineralogist, in press.
DOI: https://doi.org/10.2138/am-2023-9218. http://www.minsocam.org/

Figure 10

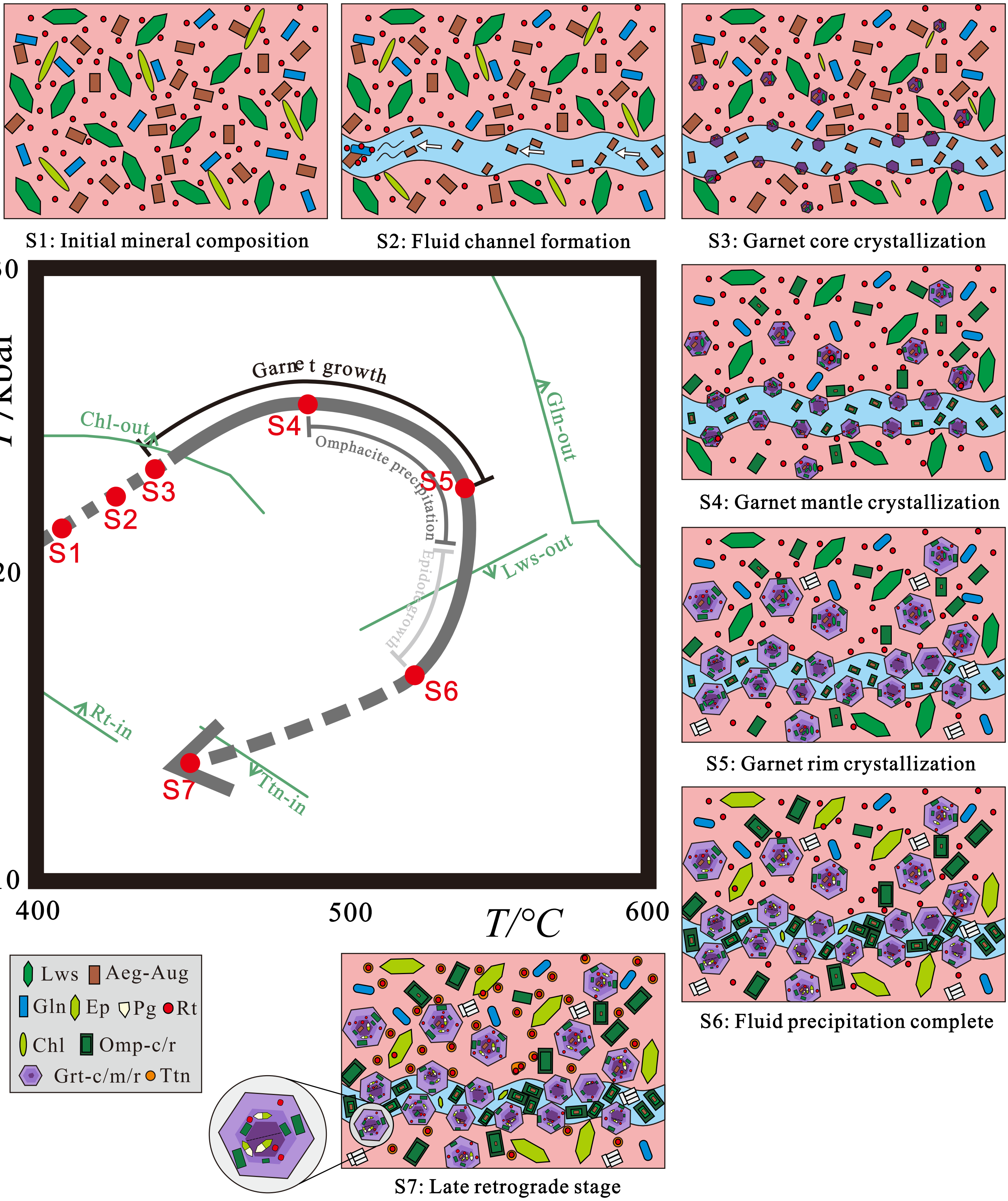

This is the peer-reviewed, final accepted version for American Mineralogist, published by the Mineralogical Society of America.
The published version is subject to change. Cite as Authors (Year) Title. American Mineralogist, in press.
DOI: https://doi.org/10.2138/am-2023-9218. http://www.minsocam.org/

Figure 11

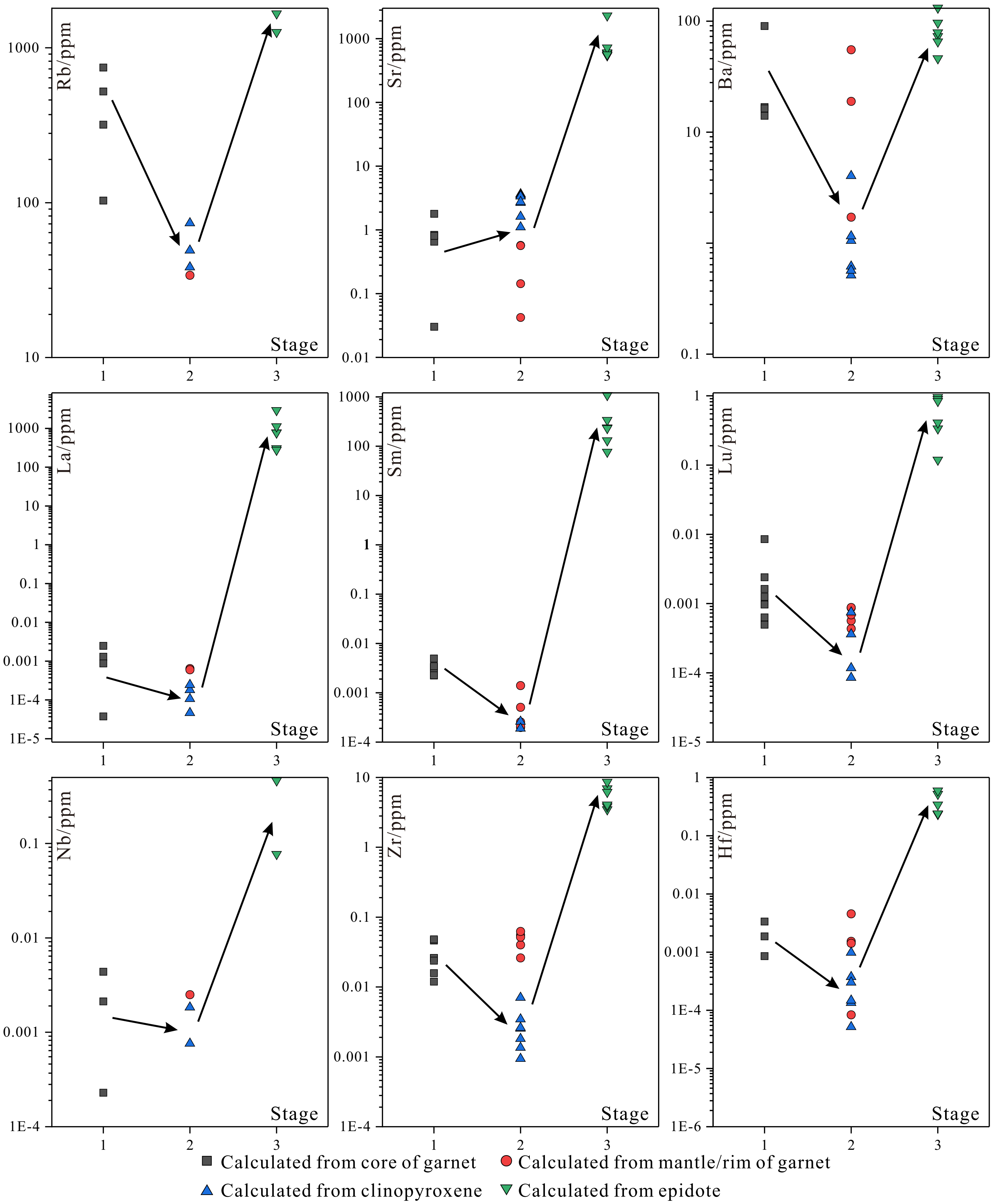

This is the peer-reviewed, final accepted version for American Mineralogist, published by the Mineralogical Society of America.
The published version is subject to change. Cite as Authors (Year) Title. American Mineralogist, in press.
DOI: https://doi.org/10.2138/am-2023-9218. http://www.minsocam.org/

Figure 12

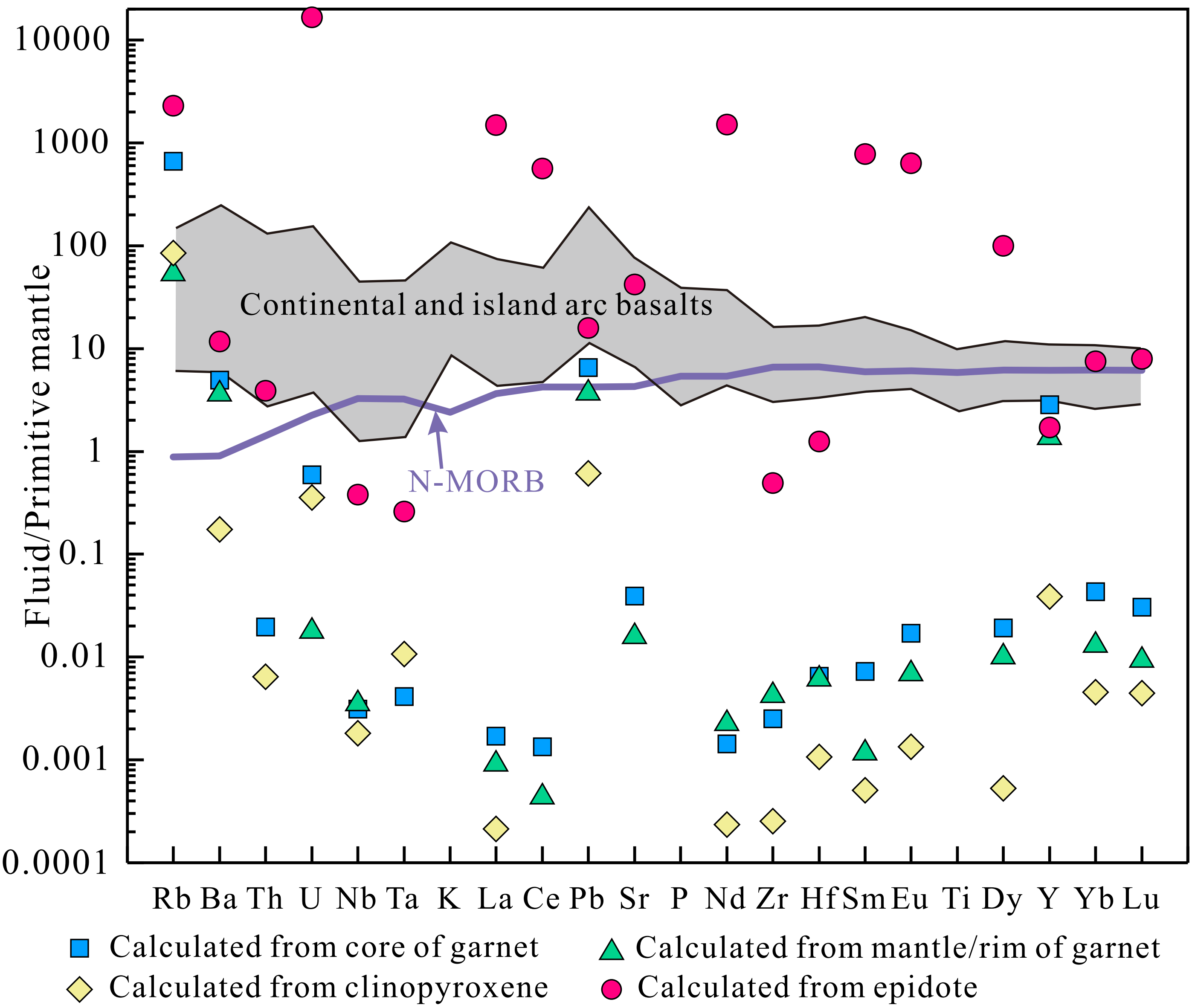

Figure 13

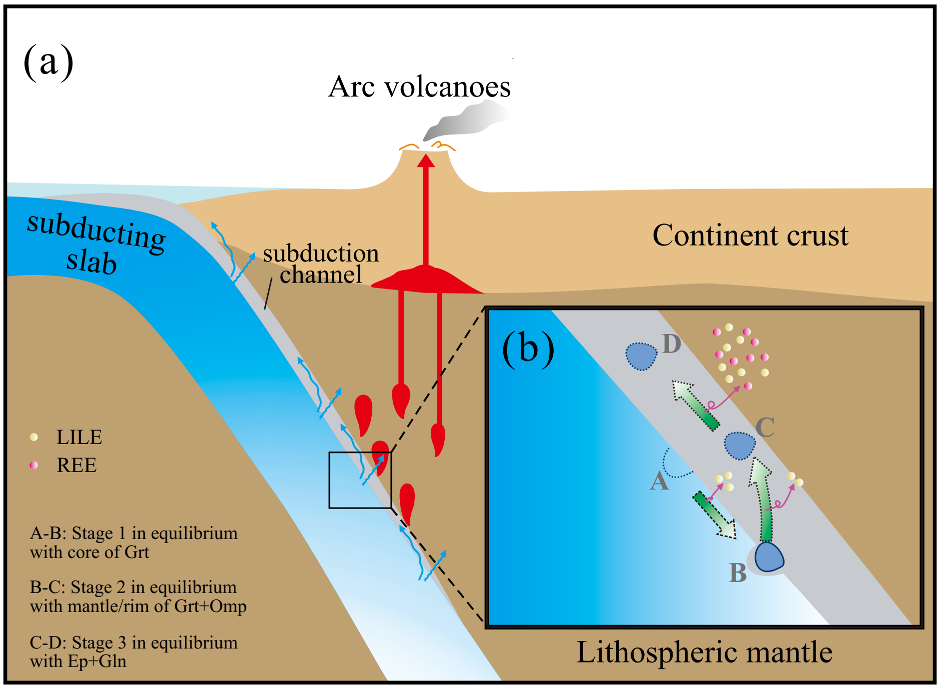
(a)
Arc volcanoes
subducting slab
subduction channel
Continent crust
(b)
D
C
A
B
LILE
REE
A-B: Stage 1 in equilibrium with core of Grt
B-C: Stage 2 in equilibrium with mantle/rim of Grt+Omp
C-D: Stage 3 in equilibrium with Ep+Gln
Lithospheric mantle